Turbulent energy flux generated by shock/homogeneous-turbulence interaction

Russell Quadros[1], Krishnendu Sinha[1,†] and Johan Larsson[2]

[1]Department of Aerospace Engineering, Indian Institute of Technology Bombay, Mumbai 400076, India

[2]Department of Mechanical Engineering, University of Maryland, College Park, MD 20742, USA

High-speed turbulent flows with shock waves are characterized by high localized surface heat transfer rates. Computational predictions are often inaccurate due to the limitations in modelling of the unclosed turbulent energy flux in the highly non-equilibrium regions of shock interaction. In this paper, we investigate the turbulent energy flux generated when homogeneous isotropic turbulence passes through a nominally normal shock wave. We use linear interaction analysis where the incoming turbulence is idealized as being composed of a collection of two-dimensional planar vorticity waves, and the shock wave is taken to be a discontinuity. The nature of the postshock turbulent energy flux is predicted to be strongly dependent on the angle of incidence of the incoming waves. The energy flux correlation is also decomposed into its vortical, entropy and acoustic contributions to understand its rapid non-monotonic variation behind the shock. Three-dimensional statistics, calculated by integrating two-dimensional results over a prescribed upstream energy spectrum, are compared with available data from direct numerical simulations. A detailed budget of the governing equation is also considered in order to gain insight into the underlying physics.

Key words: isotropic turbulence, shock waves, wave–turbulence interaction

1. Introduction

The interaction with a shock wave can drastically alter the characteristics of turbulence. Compression by the shock decreases the turbulent length and time scales, and also amplifies the kinetic energy and vorticity fluctuations of the turbulence. The temperature jump across a shock leads to higher viscosity and thus enhanced turbulent dissipation downstream of the shock. Shock–turbulence interaction often generates a large amount of acoustic energy. Due to their strong directional character, shock waves impart significant anisotropy to the turbulence field.

Shock–turbulence interaction is of practical interest in many high-speed flows. It is at the heart of shock/boundary-layer interaction, which occurs in applications ranging from transonic to hypersonic Mach numbers. Postshock turbulence levels determine the extent of flow separation and the associated pressure and heat loads in such interactions. Shock/boundary-layer interactions in rocket nozzles often lead

† Email address for correspondence: krish@aero.iitb.ac.in

to unsteady side loads. They can also alter the effectiveness of control surfaces and engine intakes. Enhanced turbulent mixing due to shock waves can be beneficial in supersonic combustors.

Engineering predictions of shock/boundary-layer interaction (SBLI) in practical configurations rely on the Reynolds-averaged Navier–Stokes (RANS) approach. Conventional turbulence models, like the k–ϵ and k–ω models, often give inaccurate predictions of wall pressure, separation size and wall heat flux (Roy & Blottner 2001). This is primarily because of the underlying gradient diffusion hypothesis that fails in rapidly distorted mean flow such as shock waves. Improvements like those in the realizable k–ϵ models (Thivet *et al.* 2001), stress-limited k–ω model (Wilcox 2008) and the SST model (Menter 1994) address some of these limitations. In addition, several physics-based turbulence models have been proposed specifically for shock-dominated flows. Sinha, Mahesh & Candler (2003) model the damping effect of shock oscillations on the turbulence kinetic energy in the k–ϵ framework. In a subsequent work, Veera & Sinha (2009) model the effect of upstream temperature fluctuations on amplification of turbulence kinetic energy. The evolution of transverse vorticity fluctuations and the effect of baroclinic torques on amplification of enstrophy is studied by Sinha (2012). This led to an accurate model equation for the turbulent dissipation rate across a shock wave.

Much of the enhanced modelling is focused on Reynolds stresses, turbulence kinetic energy (TKE) and its dissipation rate. They have a direct bearing on the fluid dynamic aspects of the interaction, and hence lead to better prediction of the separation bubble size, the shock structure and the surface pressure distribution. Improvements in the overall flow topology in the interaction region can result in some limited improvement in the prediction of surface heat flux as well (Pasha & Sinha 2012). However, there is very little work directly in the area of heat transfer in shock-dominated flows, and specifically in understanding how the interaction with a shock wave alters the internal energy transport in a turbulent flow. The current work is a step in this direction.

The turbulent heat transfer is given by either the turbulent enthalpy flux $\widetilde{u_j'' h''}$ or the turbulent energy flux $\widetilde{u_j'' e''}$, where u_j is the velocity in the jth direction, h is the specific enthalpy and e is the specific internal energy of the gas. The tilde represents Favre averaging and the corresponding fluctuations are marked by double primes. The energy flux correlation represents the transport of internal energy by velocity fluctuations in a turbulent flow. It is traditionally modelled in terms of mean temperature gradient and a turbulent conductivity, which is related to the eddy viscosity via a turbulent Prandtl number Pr_T. A value of $Pr_T = 1$ can be derived from the strong Reynolds analogy proposed by Morkovin (1962). In practice, a constant value of $Pr_T = 0.89$ gives satisfactory results in flat-plate boundary-layer flows and is often used in SBLI applications.

Mahesh, Lele & Moin (1997) show that the strong Reynolds analogy is not valid across a shock wave and thus the assumption of a constant Pr_T may not be applicable to shock-dominated flows. A variable Pr_T model proposed by Xiao *et al.* (2007) is found to improve SBLI results. Similar models are proposed by Sommer, So & Zhang (1993), Brinckman, Calhoon & Dash (2007) and Goldberg *et al.* (2010). In another work, Bowersox (2009) presents the exact transport equation for the turbulent energy flux, and simplifies it to get an algebraic model in terms of gradients in mean quantities. The model is independent of the turbulent Prandtl number, but is limited to zero-pressure-gradient boundary layers. To the best of our knowledge, there is no direct study of turbulent energy flux, its governing equations and the underlying physics in shock-dominated flows.

The presence of a shock wave can significantly alter the energy transport in a turbulent flow. For example, shock impingement on a boundary layer can result in up to 400 % increase in the surface heat flux (Schulein 2006). The turbulent heat flux generated by the shock wave is possibly a key factor that results in the dramatically increased surface heating rate. The direction of the turbulent heat flux relative to the shock wave and the inclination of the shock with respect to the wall are other factors that may influence the surface heat flux. It is therefore important to know the magnitude and sign of the turbulent energy flux in the postshock flow, and the physical parameters that govern these quantities. A knowledge of the underlying physics and their characteristic scaling is crucial to developing advanced turbulence models for accurate prediction of heat flux.

In this paper, we study the evolution of the turbulent energy flux in a canonical shock–turbulence interaction (STI), where homogeneous isotropic turbulence passes through a nominally normal shock wave. The mean flow is one-dimensional and steady, and is therefore uniform upstream and downstream of the time-averaged shock wave. This is a fundamental problem that isolates the effect of a shock wave on turbulence. It eliminates other effects like boundary-layer gradients, flow separation, shear layer attachment and streamline curvature, which are present in SBLI flows. In spite of the geometrical simplicity, the model problem exhibits a range of physical effects. These include turbulence anisotropy, generation of acoustic waves, baroclinic torques and unsteady shock oscillations. The availability of direct numerical simulation (DNS) data and theoretical results makes it an ideal problem in which to study the underlying physics. Physical insights obtained in this canonical problem have proved useful in developing advanced turbulence models for SBLI application; see, for example, Sinha (2012).

Different aspects of shock/homogeneous-turbulence interaction have been studied using DNS. In an early work, Lee, Lele & Moin (1993) report enhancement of TKE across weak shock waves. Lee, Lele & Moin (1997) further show the effect of shock strength on the amplification of turbulence. Mahesh *et al.* (1997) study the influence of upstream temperature fluctuations on amplification of TKE, vorticity variances and thermodynamic fluctuations. In a more recent work, Larsson & Lele (2009) simulate canonical STI for a large range of mean Mach numbers and turbulent Mach numbers, and study the evolution of Reynolds stresses and the Kolmogorov length scale across the shock. Larsson, Bermejo-Moreno & Lele (2013) consider additional DNS cases with varying Reynolds number and investigate turbulence anisotropy behind the shock. A similar DNS study is reported by Ryu & Livescu (2014), where high-resolution simulations are used to resolve the shock structure in canonical STI. As expected, all DNS data are limited to low values of Reynolds number, and have significant viscous effects.

Shock/homogeneous-turbulence interaction is also amenable to theoretical analysis such as rapid distortion theory (Durbin & Zeman 1992; Jacquin, Cambon & Blin 1993; Cambon, Coleman & Mansour 1993) and linear interaction analysis (Mahesh *et al.* 1997; Fabre, Jacquin & Sesterhenn 2001; Wouchuk, de Lira & Velikovich 2009). The latter approach, originally proposed by Ribner (1953, 1954) and Moore (1954), assumes the shock to be a discontinuity. A linear framework is used for small-amplitude disturbances, and viscous effects are neglected in the limit of infinite Reynolds number. In spite of the discrepancies in Reynolds number, the results of linear interaction analysis (LIA) have been routinely compared with DNS data, and found to match the amplification of TKE and enstrophy for a range of shock strengths (Sinha 2012; Larsson *et al.* 2013). The theory also predicts the rapid variation of

Reynolds stresses behind the shock, but fails to match the downstream anisotropy observed in the simulations (Larsson *et al.* 2013). In their recent work, Ryu & Livescu (2014) find that the downstream DNS statistics converge to the LIA solutions as the turbulent Mach number becomes very small, even at low values of Reynolds number.

Reynolds-averaged Navier–Stokes studies of canonical shock–turbulence interaction focus mostly on the amplification of TKE (Sinha *et al.* 2003; Veera & Sinha 2009) and its dissipation rate (Sinha 2012). Amplification and anisotropy of Reynolds stress have also been investigated (Griffond, Soulard & Souffland 1993). The majority of the work uses LIA solutions and DNS data as either a benchmark for model evaluation or limiting cases for model development. In some cases, detailed analysis of the LIA results has been used to study unclosed source terms in the turbulence model equations. Closure approximations based on the LIA results have led to advanced turbulence models for shock-dominated flows. Most notable is the shock-unsteadiness model proposed by Sinha *et al.* (2003), mentioned earlier. Here, modelling the damping effect caused by the turbulence-induced shock oscillations results in a close match of TKE prediction with DNS. The shock-unsteadiness modification was implemented in commonly used one- and two-equation turbulence models and applied to SBLI flows. Results show significant improvement in predicting the separation bubble size, wall shear stress and surface pressure distribution. The model improvements are found to be consistent for different geometric configurations (Sinha, Mahesh & Candler 2005; Pasha & Sinha 2008) with varying shock angles, at both supersonic and hypersonic Mach numbers (Pasha & Sinha 2012).

In the context of heat transfer, the current work investigates the evolution of the streamwise turbulent energy flux at a normal shock. The correlation represents transfer of energy in the shock-normal direction, and can directly influence the surface heat flux in SBLI, depending on the inclination of the shock wave. We consider arguably the simplest interaction, where the upstream disturbance field is purely vortical, without any thermodynamic fluctuations, and use LIA to study the generation of the turbulent energy flux at the shock wave. In this approach, the upstream turbulence field is represented as a collection of two-dimensional plane waves of varying intensity, wavenumber and frequency. Each planar disturbance wave interacts independently with the shock wave, and generates a set of downstream fluctuations. The upstream and downstream disturbances are characterized in terms of acoustic, entropy and vortical modes (Kovasznay 1953). The amplitudes and wavenumbers of the downstream waves are calculated by solving the linearized Euler equations behind the shock, with the linearized Rankine–Hugoniot relations applied across the shock wave. A superposition of the downstream waves, for a chosen upstream energy spectrum, gives the turbulence statistics behind the shock wave.

As a starting point, we study the elementary interaction of a single planar vortical wave with a normal shock. The effects of upstream mean flow Mach number and the wave's angle of incidence on the turbulent energy flux are investigated. Three-dimensional statistics, computed by integrating the single-wave contributions, are analysed for varying shock strengths. The energy flux correlation is also decomposed into its vortical, entropy and acoustic components to explain its behaviour downstream of the shock wave. A detailed description of the LIA procedure, along with physical interpretation of the key concepts, is presented in § 2. The results pertaining to two-dimensional single-wave interaction and those for the three-dimensional spectrum upstream of the shock are described in §§ 3 and 4, respectively. The linear theory results for three-dimensional turbulence are compared
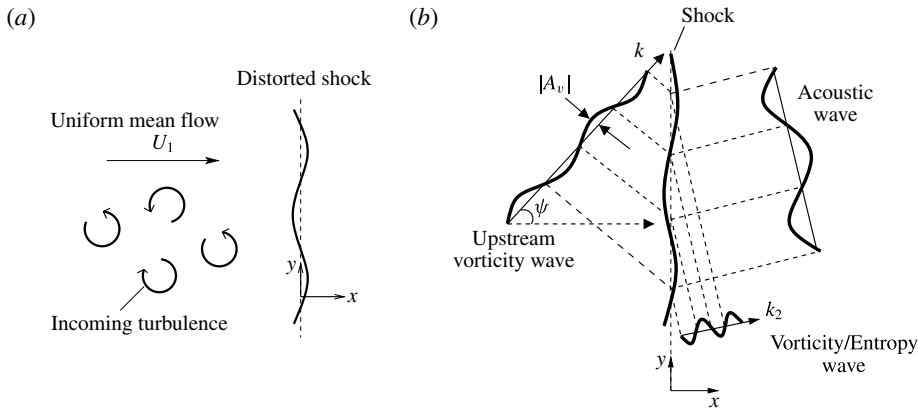
FIGURE 1. Flow description. (*a*) Schematic showing a normal shock wave distorted upon interaction with turbulent fluctuations. (*b*) A single vortical wave interacts with a shock to yield acoustic, vorticity and entropy waves downstream of the shock.

with DNS data for canonical STI in §5. The DNS data are further analysed to compute the budget of the transport equation for the turbulent energy flux in order to elucidate the dominant physical mechanisms behind a shock wave. Finally, the key observations from this work are stated in §6.

2. Formulation of the problem

A steady, one-dimensional, uniform mean flow is considered through a normal shock as shown in figure 1(*a*). The flow upstream of the shock carries a purely vortical turbulence, which is homogeneous and isotropic in nature. This turbulence can be viewed as a superposition of two-dimensional planar waves (Fourier modes) with varying wavenumbers and frequencies. The heart of the theoretical analysis, invented by Ribner (1953, 1954) and Moore (1954), and often referred to as 'linear interaction analysis', is the mathematical description of a planar wave interacting with a normal shock. The procedure adopted here follows the work of Mahesh, Lele & Moin (1996), and the parts that are directly relevant to the current work are presented for completeness. An alternative compact formulation of LIA is presented by Fabre *et al.* (2001).

Linear interaction analysis is based on the twin assumptions of linearized and inviscid evolution of disturbances. In order for LIA to accurately model reality (or DNS results), these assumptions must be satisfied both exactly at the shock and in the postshock adjustment and downstream convection regions. It is qualitatively clear that LIA should become more accurate for decreased M_t (weaker turbulence), increased M_1 (stronger shock, making the turbulence a weaker perturbation) and increased Reynolds number (decreased viscous effects). Ryu & Livescu (2014) argue that the deviation from the LIA limit can be quantified by the ratio

$$\frac{\delta}{\eta} \simeq 7.69 \frac{M_t}{M_1 - 1} \frac{1}{\sqrt{Re_\lambda}}, \tag{2.1}$$

where δ is the estimated laminar shock thickness, η is the estimated Kolmogorov length scale and Re_λ is the Reynolds number based on the Taylor microscale.

They then show how DNS results converge towards the LIA predictions as δ/η is reduced. This parameter measures the separation in length scales between the shock and the smallest turbulence eddies, and thus should be relevant to whether the LIA assumptions are satisfied at the shock. One should note that δ/η is inherently a very conservative estimate: it is plausible that a sufficient condition is that δ is smaller than some fraction of the integral scale or a similar measure of the eddies that carry the energy (rather than the smallest eddies). In that spirit, i.e., assuming that the LIA assumptions are likely to be satisfied at the shock, Larsson *et al.* (2013) focus on the viscous effects behind the shock as the main violation of the LIA assumptions, and approximately remove the viscous effects by extrapolating back to the mean shock location. They then find excellent agreement between LIA and DNS for the amplification of the turbulence kinetic energy even at relatively high values of δ/η (and relatively strong turbulence) once the viscous decay behind the shock is compensated for. This suggests that the viscous effects may be more important than the nonlinear effects, at least in the context of the amplification of turbulence kinetic energy.

The question of which parameter best describes the validity of LIA is still open. In the context of the present study, the main point is that LIA can be expected to be reasonably accurate, but that we should expect discrepancies between the LIA and DNS due to the substantial viscous effects in the latter.

2.1. *An elemental two-dimensional vorticity wave*

A single representative vortical wave upstream of the shock is shown in figure 1(*b*). This wave is characterized by a wavenumber k, an angle of incidence ψ and a complex amplitude A_v. The velocity fluctuations in the x and y directions (shown in the figure) are given by

$$\frac{u'_1}{U_1} = A_v \sin \psi \exp[\mathrm{i}k(x \cos \psi + y \sin \psi - U_1 t \cos \psi)], \qquad (2.2a)$$

$$\frac{v'_1}{U_1} = -A_v \cos \psi \exp[\mathrm{i}k(x \cos \psi + y \sin \psi - U_1 t \cos \psi)], \qquad (2.2b)$$

where U_1 is the mean velocity upstream of the shock wave. The thermodynamic fluctuations p'_1, ρ'_1 and T'_1, corresponding to pressure, density and temperature, are assumed to be identically zero. Upon interaction, the shock distorts from its mean position; the unsteady distorted shock wave is given by $\xi(y, t)$. The temporal derivative of the shock deviation ξ_t represents the local streamwise velocity of the shock wave, and the transverse derivative ξ_y describes the angular distortion of the shock (see Sinha (2012) for further details).

The wave amplitudes are assumed to be small in magnitude as compared to the changes in the mean flow quantities across the shock. The interaction of the waves with the shock and their downstream evolution is therefore studied in a linear framework. Furthermore, viscous effects are neglected, and the shock is modelled as a discontinuity. The linearized Rankine–Hugoniot conditions are used to relate the shock-upstream (subscript 1) disturbances to the shock-downstream (subscript 2) values as

$$\frac{u'_2 - \xi_t}{U_1} = B\frac{u'_1 - \xi_t}{U_1}, \quad \frac{v'_2}{U_1} = \frac{v'_1}{U_1} + E\xi_y, \quad \frac{\rho'_2}{\overline{\rho}_2} = C\frac{u'_1 - \xi_t}{U_1}, \quad \frac{p'_2}{\overline{p}_2} = D\frac{u'_1 - \xi_t}{U_1}, \quad (2.3a\text{--}d)$$

where B, C, D and E are functions of upstream mean flow Mach number M_1 and the ratio of specific heats γ of the gas, and are described in appendix A. Throughout this work, the value of γ is taken as 1.4.

The disturbance behind the shock consists of a refracted vortical wave, an entropy wave and an acoustic wave (figure 1b). The vorticity and the entropy wave are stationary with respect to the mean flow downstream of the shock. The acoustic wave propagates at the speed of sound relative to the mean flow. The associated streamwise velocity and temperature fluctuations take the form

$$\frac{u'_2}{U_1} = A_v\{\widetilde{F}\exp(i\widetilde{k}x) + \widetilde{G}\exp(ikrx\cos\psi)\}\exp[ik(y\sin\psi - U_1 t\cos\psi)], \quad (2.4a)$$

$$\frac{T'_2}{\overline{T}_2} = A_v\left\{\frac{\gamma-1}{\gamma}\widetilde{K}\exp(i\widetilde{k}x) - \widetilde{Q}\exp(ikrx\cos\psi)\right\}\exp[ik(y\sin\psi - U_1 t\cos\psi)]. \quad (2.4b)$$

The wavenumber in the shock-transverse direction and the frequency match those of the upstream wave, whereas the x-direction wavenumber is modified across the shock. The complex coefficients $\widetilde{F}$ and $\widetilde{K}$ (representing the amplitude and phase) correspond to the acoustic mode, while $\widetilde{G}$ and $\widetilde{Q}$ correspond to the vortical and entropy modes, respectively. The mean density ratio across the shock is given by r and the x-component of the acoustic-mode wavenumber is $\widetilde{k}$.

Similar expressions can be written for other postshock variables and the instantaneous shock speed. For example,

$$\frac{\xi_t}{U_1} = A_v\widetilde{L}\exp[ik(y\sin\psi - U_1 t\cos\psi)], \quad (2.5)$$

where $\widetilde{L}$ is the associated complex amplitude. The downstream solution can be obtained by substituting the fluctuating variables in the governing equations (linearized Euler and linearized Rankine–Hugoniot) and solving the resulting algebraic equations. This yields the values of the complex amplitudes; details are provided in appendix A.

2.2. *Postshock acoustic field*

The characteristics of the downstream acoustic field are determined by the wavenumber $\widetilde{k}$ obtained as part of the solution procedure. The acoustic waves propagate with a constant amplitude (for real $\widetilde{k}$) or decay with streamwise distance (for complex $\widetilde{k}$). The nature of the acoustic waves is crucial to the interaction; this can most easily be understood by adopting a coordinate transformation suggested by Ribner (1953), in which the unsteady interaction of a plane vorticity wave with a normal shock is transformed into an equivalent steady interaction of the disturbance wave with an oblique shock. This is achieved by adding a mean velocity component such that the total mean velocity is in the direction parallel to the incoming wavefronts, as shown in figure 2. In the transformed problem, the shock wave makes an angle ψ with the upstream mean flow, and the flow downstream of the shock can be either subsonic or supersonic depending on the value of ψ. The nature of the acoustic field will change dramatically between these cases.

For small angles ψ (for a fixed M_1), the flow behind the shock is supersonic in the transformed problem. The acoustic waves generated downstream of the shock propagate radially at the speed of sound while they are convected by the local fluid
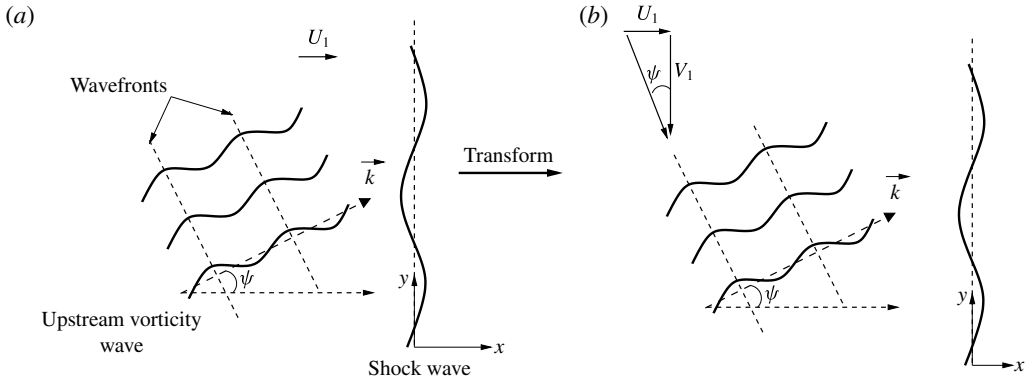
FIGURE 2. An unsteady problem of an upstream vorticity wave interacting with a normal shock, transformed into a steady interaction with an oblique shock.
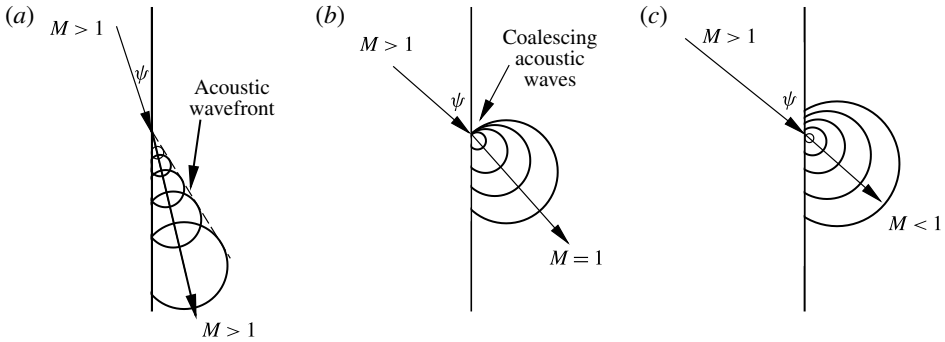

FIGURE 3. The acoustic wave patterns downstream of the shock in the transformed coordinate system for three upstream wave angles: (*a*) $\psi < \psi_c$ (propagating regime), (*b*) $\psi = \psi_c$ (critical angle) and (*c*) $\psi > \psi_c$ (decaying regime).

velocity. A conical pattern of the downstream disturbance is thus formed, as sketched in figure 3(*a*), and the common tangent to the circular wave patterns represents the wavefront of the acoustic disturbance. The two-dimensional planar wavefronts propagate with a constant amplitude in the downstream region. This qualitative behaviour is termed the 'propagating regime'.

For large values of ψ, the flow downstream of the shock is subsonic in the transformed problem. The acoustic waves generated at the shock expand radially outwards at sonic speed while being convected subsonically; this is sketched in figure 3(*c*). The ever expanding circles do not add up along a common tangent, and the amplitude of the acoustic wave decays with distance from the shock. This regime is therefore termed the 'decaying regime'.

For every upstream Mach number M_1, there exists a critical angle $\psi = \psi_c$ for which the downstream transformed flow is sonic. Geometrically, this is given as (Ribner 1953)

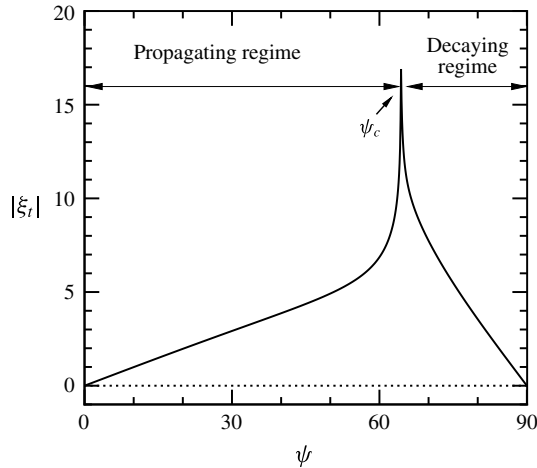$$\psi_c = \tan^{-1}\left(\frac{rM_2}{\sqrt{1-M_2^2}}\right),\qquad(2.6)$$

FIGURE 4. Amplitude of shock speed plotted as a function of upstream wave angle ψ (in degrees) for the case of $M_1 = 3$. The amplitude is normalized by the upstream mean velocity and $|A_v|$.

where M_2 is the downstream Mach number in the original unsteady (i.e., normal shock) problem. The acoustic waves at the critical angle are sketched in figure 3(*b*). For such a case, the pressure wave patterns not only propagate radially outward at the speed of sound but are also convected at that speed. The downstream acoustic disturbances therefore accumulate at the shock, leading to high values of downstream fluctuations, including local shock speed and distortion. See, for example, figure 4 plotted for $M_1 = 3$, where the amplitude of the shock speed reaches a peak value as ψ approaches the critical angle. It is to be noted that, for such high values of fluctuations in the vicinity of ψ_c, the linear assumptions may not hold, and the theoretical predictions may be inaccurate (Mahesh *et al.* 1996).

2.3. *Near-field/far-field distinction*

Figure 5 shows the variation of streamwise Reynolds stress $\overline{u'^2}$ and internal energy variance $\overline{e'^2}$ for a single-wave interaction with a Mach 1.5 shock wave. The turbulent correlations are computed as $\overline{u'^2} = \overline{u'u'^*}$ and $\overline{e'^2} = c_v^2 \, \overline{T'T'^*}$ using (2.2) for the upstream flow and (2.4) along with the complex coefficients given in appendix A for the downstream field. Here, * indicates complex conjugate and $c_v = R/(\gamma - 1)$ is the specific heat of the gas at constant volume. Conventional Reynolds averaging is used, instead of Favre averaging for compressible flows, because the difference between the two is negligible in the linear framework.

The LIA results plotted in figure 5 are normalized as per Mahesh *et al.* (1997). The velocity fluctuations, both upstream and downstream, and the shock speed are non-dimensionalized by the upstream mean velocity U_1. The thermodynamic fluctuations downstream of the shock are non-dimensionalized by the respective mean values in the postshock flow. The specific gas constant R is used to non-dimensionalize the specific heats. Further, the magnitude of the downstream fluctuations and the shock speed are proportional to the amplitude of the upstream vortical wave (see, for example, (2.5)). The correlations plotted in figure 5 are therefore normalized by the turbulence kinetic energy upstream of the shock wave. The same is true for the turbulent energy flux and
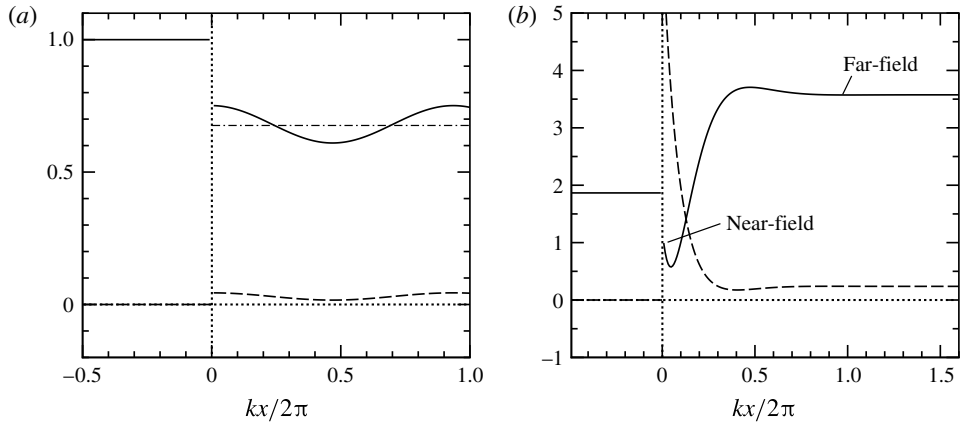
FIGURE 5. Variation of $\overline{u'^2}$ (solid) and $\overline{e'^2}$ (dashed) with streamwise distance for $M_1 = 1.5$ and upstream angle of incidence (a) $\psi = 45°$ (propagating regime) and (b) $\psi = 75°$ (decaying regime). In the propagating regime, $\overline{u'^2}$ oscillates about a mean value (dash-dotted). The velocity fluctuations are normalized by the upstream mean velocity and the energy fluctuations are normalized by the product of downstream mean temperature and the specific gas constant R. All correlations are further normalized by the upstream TKE.

other quantities presented in the following sections. In the absence of a physical shock thickness in LIA, the preshock disturbance wavelength $2\pi/k$ serves as the governing characteristic length. This is used to normalize the streamwise coordinate in figure 5 and other subsequent figures.

The upstream field is purely vortical and results in a uniform $\overline{u'u'}$ prior to the shock, located at $x = 0$. In the absence of thermodynamic fluctuations, $\overline{e'e'}$ is identically zero in the upstream flow. The downstream Reynolds stress has contributions from the refracted vortical wave and the acoustic wave generated at the shock. The two components have different wavenumbers and their correlation exhibits a sinusoidal variation in the downstream flow. This can be seen prominently in figure 5(a), where $\psi = 45°$, and the interaction lies in the propagating regime. The downstream waves propagate at a constant amplitude, and the postshock state remains unchanged far away from the shock (in the linear and inviscid framework). The internal energy variance also shows a sinusoidal trend, but with a relatively small amplitude, behind the shock.

The data plotted in figure 5(b) correspond to $\psi = 75°$, which lies in the decaying regime. The Reynolds stress in this case shows a rapid non-monotonic variation from a low positive value (at $x = 0$) to a high asymptotic level beyond $x \simeq \pi/k$. This trend is due to the streamwise decay in acoustic energy generated at the shock, with the far-field contribution to the Reynolds stress primarily from the vorticity mode; see Mahesh *et al.* (1997) for further details. The amplitudes and correlations obtained immediately behind the shock (taken as a discontinuity) are identified as the near field. By comparison, the far field is defined as the asymptotic value obtained away from the shock at distances where the acoustic mode has become negligible in magnitude. We note that the $\overline{e'e'}$ correlation takes a high near-field value just across the shock and decays exponentially to a low far-field value, once again due to the decay of the acoustic part of the internal energy fluctuations.

Homogeneous isotropic turbulence is a collection of two-dimensional waves with all possible orientations, and this will always include modes in the decaying regime.
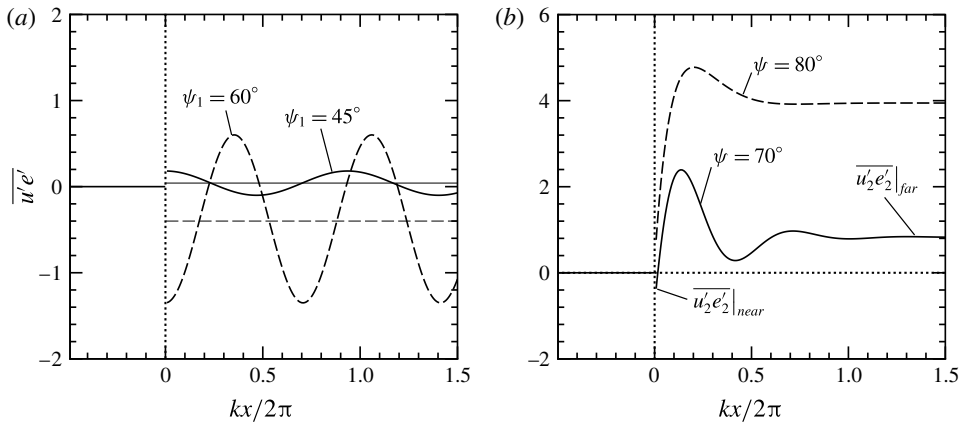
FIGURE 6. Streamwise variation of $\overline{u'e'}$ generated by a planar vortical wave interacting with a normal shock: (*a*) propagating regime, $M_1 = 1.5$, and (*b*) decaying regime, $M_1 = 3$. Normalization is as described in figure 5.

Therefore, the distinction between the near field and the far field must be made for three-dimensional turbulence as well. It is important to consider the distinction between the near field and the far field in the context of realistic applications. More specifically, one should ask the question whether the near-field results are important or not in a shock/boundary-layer interaction? The rapid near-field variations are seen over a streamwise extent of about π/k behind the shock. For three-dimensional turbulence, this implies a distance of approximately half the size of the largest scales, which are of the order of the boundary-layer thickness. As a consequence, it is plausible that the near-field effects behind the shock are important in determining the postshock relaxation and reattachment, as well as the heat transfer rates in this region, in a typical shock/boundary-layer interaction. We therefore analyse both the near- and far-field values of the turbulent energy flux in the present study.

3. Single-wave interaction results

A normalized expression for the turbulent energy flux is given by

$$\overline{u'_2 e'_2} = \left(\frac{1}{\gamma - 1} \right) \frac{1}{U_1 \overline{T}_2} \frac{\left[\overline{u'_2 T'^*_2} + \overline{T'_2 u'^*_2} \right]}{2(\text{TKE}_1 / U_1^2)}, \tag{3.1}$$

where the expressions for u'_2 and T'_2 are given in (2.4), and TKE_1 represents the shock-upstream turbulence kinetic energy. Unless specified otherwise, all values of turbulent energy flux described in this work are normalized in this manner.

Figure 6(*a*) shows the streamwise variation of the turbulent energy flux for plane wave disturbances incident at 45° and 60° on a Mach 1.5 normal shock wave. The energy flux values upstream of the shock are identically zero, as expected for a purely vortical disturbance field interacting with a shock wave. Both cases are in the propagating regime ($\psi < \psi_c$ for $M_1 = 1.5$), and the energy flux correlation shows no streamwise decay. The qualitative trend is similar to that presented in figure 5(*a*). For the lower angle of incidence of 45°, the downstream energy flux varies sinusoidally about a small positive mean, with the highest positive value obtained at the shock

wave. The postshock value attained at $x = 0$ is the near-field energy flux correlation. For the 60° case, the correlation has peak negative value at the shock wave, and it oscillates about a negative mean far-field value. The sign of the correlation determines the direction of internal energy transfer due to turbulent mixing. Positive values of near-field $\overline{u'_2 e'_2}$ indicate energy transfer away from the shock, as in the case of $\psi = 45°$. By comparison, a negative turbulent energy flux, for $\psi = 60°$, implies that the turbulent energy transfer is back towards the shock wave.

The turbulent energy flux generated by interactions in the decaying regime is shown in figure 6(*b*). The data correspond to angles of incidence of 70° and 80° for an upstream Mach number of 3, where a stronger shock wave generates much higher energy flux values than those in figure 6(*a*). For $\psi = 70°$, the correlation starts with a negative near-field value just across the shock, then shows a rapid increase to a positive peak followed by a non-monotonic decay to an asymptotic far-field value. We note that the net energy transport in the shock-normal direction is proportional to the streamwise derivative of the turbulent energy flux. Decaying interactions yield a high gradient in $\overline{u'e'}$ behind the shock, which can lead to a rapid redistribution of the postshock energy in this region. This is in contrast to the energy flux generated by interactions in the propagating regime, where the sinusoidal variation of $\overline{u'e'}$ about a mean value results in zero net transport of energy over a wavelength.

The variation of the turbulent energy flux for $\psi = 80°$ is similar to that described above. The correlation has a higher peak value followed by a relatively higher far-field level compared to that at the lower angle of incidence. Unlike the 70° case, $\overline{u'e'}$ is positive immediately behind the shock for the 80° interaction. Thus, the energy flux correlation takes distinct positive and negative values in the near field and far field for the different cases presented above. Its magnitude also changes significantly depending on the strength of the shock wave and the angle of incidence of the upstream disturbance wave. In the subsequent part, we study the variations in $\overline{u'e'}$ over the entire ψ range for varying M_1. The wave patterns generated at the shock and their contribution towards the energy flux correlation, both in the near field and the far field, are presented in detail.

3.1. *Near-field analysis*

Figure 7(*a*) shows the near-field values of the turbulent energy flux for a range of upstream Mach numbers and angles of incidence. The critical angle ψ_c, given by (2.6), is plotted as a function of M_1, and peak negative values of the turbulent energy flux are observed in the vicinity of this curve (darker shade). This is because of the high values of the velocity and the temperature fluctuations generated by interactions at the critical angle, as discussed in the previous section.

The zone of negative correlation is bounded by the ψ_z curve in the propagating regime and by the ψ_o curve in the decaying regime. The flow physics at the angles of incidence ψ_z and ψ_o is described subsequently. The unshaded part of the $M_1-\psi$ domain in figure 7(*a*) corresponds to positive $\overline{u'_2 e'_2}$ immediately behind the shock. A few representative contour lines are plotted for reference, and it is noted that the positive values of the energy flux are much smaller in magnitude than the peak negative values obtained at the critical angle of incidence.

The variation of the energy flux correlation with Mach number is plotted for three representative values of the angle of incidence in figure 7(*b*). This corresponds to the data extracted along lines with $\psi =$ constant in figure 7(*a*). The case with $\psi = 45°$ shows positive turbulent energy flux for the entire range of Mach numbers, with $\overline{u'_2 e'_2}$
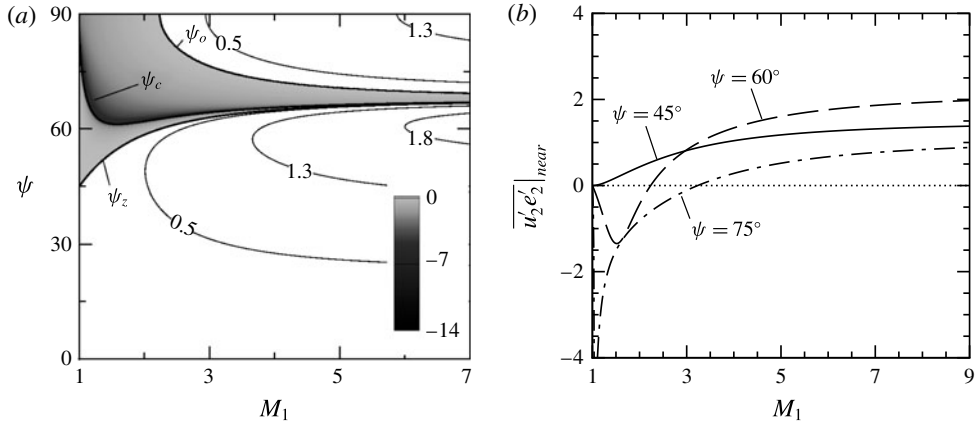
FIGURE 7. Near-field turbulent energy flux generated by a single-wave interaction. (*a*) Contours of $\overline{u'_2 e'_2}$ across the M_1–ψ domain, with negative correlation shown in greyscale. The critical angle ψ_c separating the propagating and decaying regimes is plotted along with the angles ψ_z and ψ_o, for which the correlation is zero in the propagating and decaying regimes, respectively. (*b*) Variation of near-field $\overline{u'_2 e'_2}$ for three representative angles of incidence. Normalization is as described in figure 5.

reaching an asymptotic value at high Mach numbers. The energy flux correlation takes vanishingly small values in the limit $M_1 \to 1$, as negligible temperature fluctuations are generated across a very weak shock wave. For the case $\psi = 60°$, the energy flux correlation is negative for relatively weak shocks ($M_1 < 2.25$) and increases to a positive limiting value as $M_1 \to \infty$. Both $\psi = 45°$ and $\psi = 60°$ are lower than the least value of $\psi_c \sim 61°$ (obtained at Mach 1.5) and therefore lie in the propagating regime for all Mach numbers.

The near-field turbulent energy flux for $\psi = 75°$ plotted in figure 7(*b*) shows large negative values in the vicinity of Mach 1. This is because of the fact that the critical angle ψ_c equals 75° for $M_1 = 1.04$, and a large negative value of $\overline{u'_2 e'_2} = -4.77$ is obtained at this Mach number. The magnitude of correlation then drops rapidly to zero in the limit $M_1 \to 1$. Note that the 75° interactions for $M_1 > 1.04$ lie in the decaying regime, and both positive and negative turbulent energy flux values are generated depending on the mean flow Mach number. Negative $\overline{u'_2 e'_2}$ correlation is confined to Mach numbers below 3 and positive values are obtained for stronger shock waves.

3.1.1. *Nature of fluctuations in the propagating regime*

Consider a plane vorticity wave incident at 45° on a Mach 1.5 shock wave. For this case, LIA predicts that all three downstream waves (vorticity, entropy and acoustic) are in phase with each other and with the upstream vorticity wave. The downstream disturbances such as u'_2 and e'_2, with contributions from the three modes, are also in phase with the upstream streamwise fluctuation u'_1. This can be seen in figure 8(*a*), where u'_1 is plotted along with u'_2 and e'_2 as a function of time in the immediate vicinity ($x = 0$) of the instantaneous shock wave. For this interaction, the correlation $\overline{u'_2 e'_2}$ is positive, as both the constitutive fluctuations are in phase.

Figure 8(*b*) plots the LIA solution for the fluctuations at $x = 0$ for $\psi = 60°$ and $M_1 = 1.5$. In this case, the velocity fluctuations, u'_2 and u'_1, are in phase with each
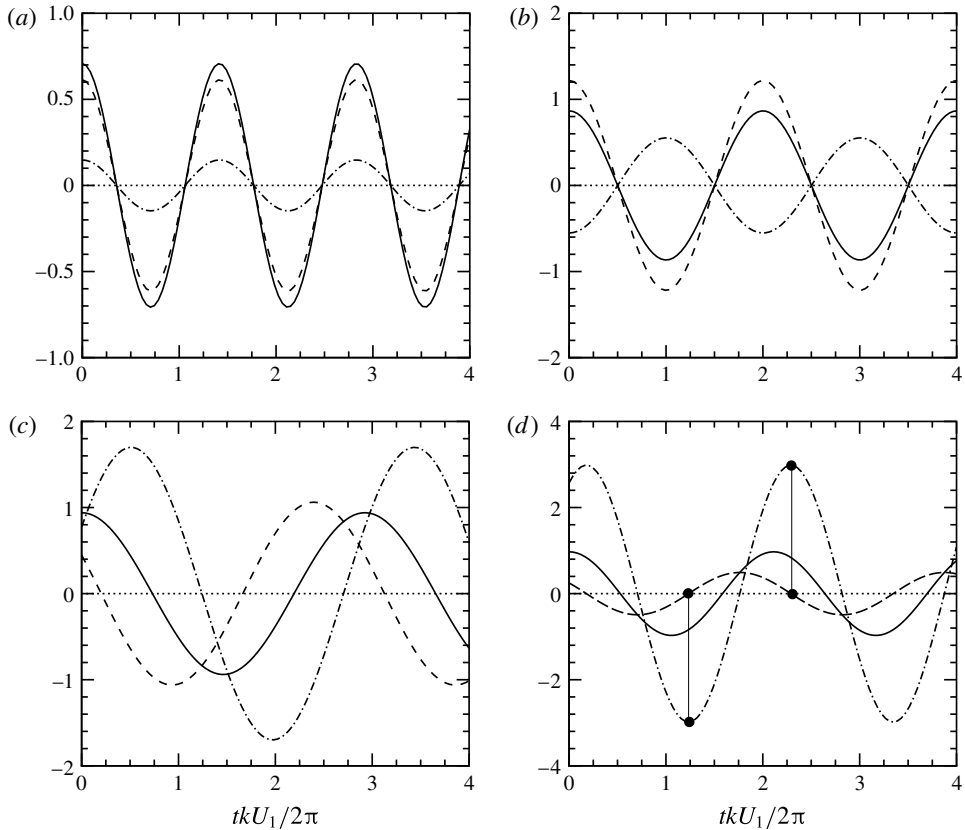
FIGURE 8. Near-field variation of the fluctuating variables with time: u'_1 (solid), u'_2 (dashed) and e'_2 (dash-dotted). (a) $\psi = 45°$, (b) $\psi = 60°$ and (c) $\psi = 70°$ for the case of $M_1 = 1.5$, and (d) $\psi = \psi_\circ = 76.3°$ at $M_1 = 3$. Velocity fluctuations are normalized by the upstream mean velocity and energy fluctuation is normalized by the downstream mean temperature and R. All fluctuations are normalized by $|A_v|$.

other, but e'_2 has an opposite phase to the velocity fluctuations. Thus, the correlation $\overline{u'_2 e'_2}$ takes a negative value with the constituting fluctuations having a phase difference of π. Note that the postshock u' and e' fluctuations are exactly in opposite phase for all propagating interactions with $\psi > \psi_z$, whereas the downstream fluctuations are in phase for lower angles of incidence ($\psi < \psi_z$). The ψ_z curve in the M_1–ψ plot in figure 7(a) thus demarcates the single-wave interactions that generate positive and negative energy flux correlations in the propagating regime.

Interestingly, plane wave vortical disturbances incident on a shock at an angle of ψ_z generate vanishingly small energy flux downstream. For this unique angle ψ_z, it is found that the shock oscillations are in phase with the upstream velocity fluctuations, and the instantaneous shock speed matches the fluctuating streamwise velocity ($\xi_t = u'_1$). Thus, there are no apparent streamwise disturbances in the flow relative to the unsteady shock, and the shock-normal velocity fluctuations pass unchanged through the shock wave ($u'_1 = u'_2$). The vorticity wave refracts through the shock and there is a change in the transverse velocity fluctuations. No acoustic or entropy waves are generated behind the shock for this case of $\psi = \psi_z$, resulting in a zero value of $\overline{u'_2 e'_2}$.

An analytical expression for ψ_z can be obtained by equating the expressions for the shock speed and the streamwise velocity fluctuation just ahead of the shock. Equations (2.2a) and (2.5) thus yield for $x = 0$

$$\sin \psi = \widetilde{L}. \tag{3.2}$$

The full expression for $\widetilde{L}$ is provided in (A 2). In the current limiting case of $\psi = \psi_z$ with $\alpha = 0$ and $\beta = \tan \psi / (\gamma M_2^2 r^2)$, the expression for $\widetilde{L}$ reduces to

$$\widetilde{L} = \frac{-\cos\psi - \beta D \sin \psi + rB \cos \psi}{E \tan \psi - \beta D - r(1 - B) \cot \psi}. \tag{3.3}$$

Substituting the above expression in (3.2) results in

$$E \tan^2 \psi_z = r - 1, \tag{3.4}$$

which simplifies to

$$\psi_z = \tan^{-1} \sqrt{r}. \tag{3.5}$$

Thus, ψ_z is a function of the mean density ratio across the shock wave, which in turn depends on the upstream mean flow Mach number and the ratio of specific heats. It starts from a value of 45° for $M_1 = 1$ and asymptotes to a value close to ψ_c in the limit of $M_1 \to \infty$ (see figure 7a). Thus, a vorticity wave incident at angles less than 45° generates positive $\overline{u_2' e_2'}$ behind the shock for all Mach numbers. Also, in the hypersonic limit, almost all the waves in the propagating regime, except for a small range near ψ_c, result in a positive energy flux correlation in the near field.

The temporal variation of u_2' and e_2' plotted in figure 8 provides further insight into the energy transfer taking place immediately behind the shock wave. The data for $\psi = 45°$ show that positive streamwise velocity fluctuations are concurrent with locally higher internal energy, thus resulting in an energy transfer in the positive x direction, i.e. away from the shock wave. For the angle of incidence of 60°, on the other hand, higher streamwise velocity transports locally cooler fluid, with negative internal energy fluctuation, in the positive x direction. This is equivalent to an effective turbulent energy flux back towards the shock wave. For the special case of ψ_z without any entropy and acoustic waves generated at the shock, the downstream internal energy is uniform and the velocity fluctuations have no effect on the energy transport in the shock-normal direction.

3.1.2. *Nature of fluctuations in the decaying regime*

Figure 8(c) plots u_1', u_2' and e_2' at the shock as a function of time for $\psi = 70°$ at Mach 1.5, which lies in the decaying regime. In this case, the downstream velocity fluctuation appears to lag behind its upstream counterpart, while the postshock internal energy fluctuations lead the upstream wave. The energy flux correlation is given by

$$\overline{u_2' e_2'} = |u_2'||e_2'| \cos \phi_{ue}, \tag{3.6}$$

where ϕ_{ue} is the phase difference between the near-field streamwise velocity and the internal energy fluctuations. The variation of $\cos \phi_{ue}$ with the upstream angle of incidence is plotted in figure 9 for two Mach numbers. In the propagating regime, the velocity and energy fluctuations are either in phase ($\psi < \psi_z$) or exactly in opposite phase ($\psi > \psi_z$). By comparison, the phase difference ϕ_{ue}, for interactions
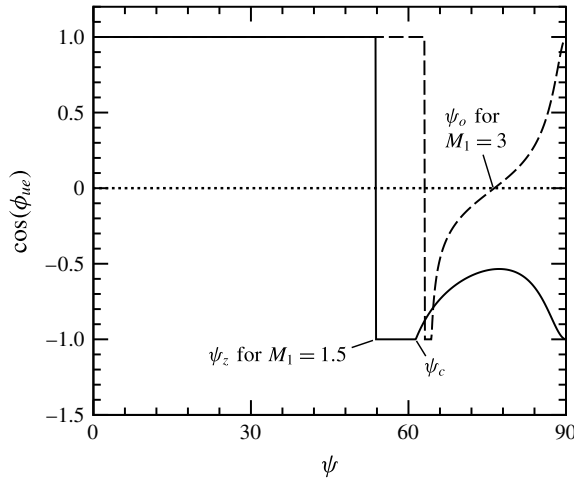
FIGURE 9. Cosine of the phase difference between near-field u_2' and e_2' for an upstream Mach number of $M_1 = 1.5$ (solid) and $M_1 = 3$ (dashed) as a function of upstream wave angle (in degrees).

in the decaying regime, varies continuously over a range of values. For the case of $M_1 = 1.5$, when the angle of incidence is increased beyond ψ_c, the phase difference decreases from π to reach a minimum value before increasing back to π for $\psi = 90°$. The correlation $\overline{u_2' e_2'}$ is negative for all decaying interactions at this Mach number (see figure 7a), and this is true for relatively weak shocks ($M_1 < 2.2$).

At higher Mach numbers, the correlation switches back from negative to positive values at a high upstream angle of incidence. This can be seen for the case of $M_1 = 3$, where the phase difference ϕ_{ue} crosses $\pi/2$ at an angle of incidence of ψ_o, and decreases further to zero at $\psi = 90°$. The disturbance waves plotted for $\psi = \psi_o = 76.3°$ at $M_1 = 3$ in figure 8(d) show this effect clearly. The nodes in the downstream velocity wave in this case coincide with the peaks in the internal energy wave, and vice versa. The near-field energy flux correlation thus vanishes, in spite of the large internal energy fluctuations generated by the shock. This is unlike the angle of incidence of ψ_z in the propagating regime, where a zero energy flux is caused by the fact that no energy fluctuations are generated at the shock wave.

At the critical angle of incidence, the near-field turbulent energy flux is negative for all Mach numbers. For this case, the complex coefficients used in defining the postshock streamwise velocity and temperature fluctuations, namely $\widetilde{F}$, $\widetilde{G}$, $\widetilde{K}$ and $\widetilde{Q}$, given by (A 6), have the following form

$$\left.\begin{array}{c} \widetilde{F} = \dfrac{D}{\gamma r} \sin \psi_c, \quad \widetilde{G} = \left(2 - B - \dfrac{D}{\gamma r}\right) \sin \psi_c, \\[2mm] \widetilde{K} = -D \sin \psi_c, \quad \widetilde{Q} = \left(\dfrac{D}{\gamma} - C\right) \sin \psi_c, \end{array}\right\} \tag{3.7}$$

where the Rankine–Hugoniot coefficients are given in (A 1), and ψ_c can be calculated from (2.6) for a given upstream mean flow Mach number. The near-field value of the $\overline{u_2' e_2'}$ correlation, thus computed, is plotted for a range of upstream Mach numbers in figure 10 and it shows a non-monotonic behaviour leading to a limiting value for $M_1 \to \infty$.
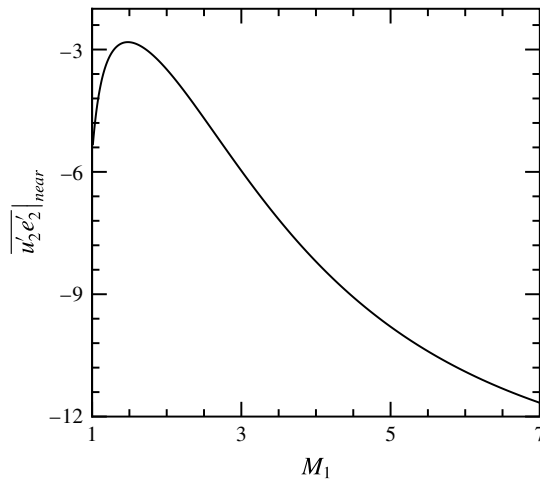
FIGURE 10. Near-field peak negative turbulent energy flux generated by single-wave interaction at the critical angle, plotted as a function of upstream Mach number. Normalization is as described in figure 5.
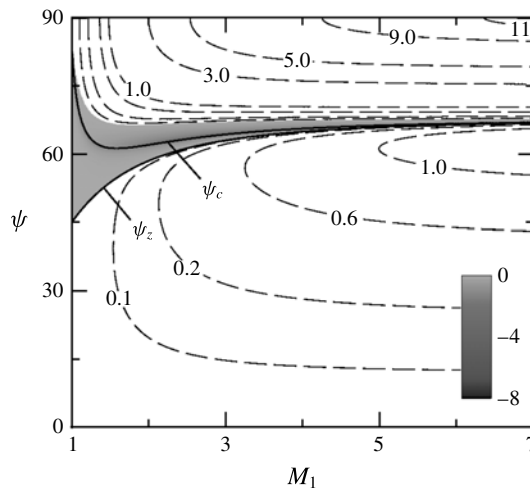

FIGURE 11. Far-field turbulent energy flux correlation obtained for varying upstream Mach number and angle of incidence of the wave. Normalization is as described in figure 5.

3.2. *Far-field analysis*

The far-field values of the turbulent energy flux obtained from LIA applied to single plane waves interacting with a normal shock are plotted in figure 11. As earlier, the shaded part of the M_1–ψ domain indicates the region of negative $\overline{u_2' e_2'}$, and the positive values are shown using representative contour lines. The critical angle ψ_c is also shown, with $\psi < \psi_c$ representing the propagating regime. The far-field value of $\overline{u_2' e_2'}$ for a wave in the propagating regime is taken as the mean value about which the sinusoidal variation exists. This is based on the fact that the oscillating part of
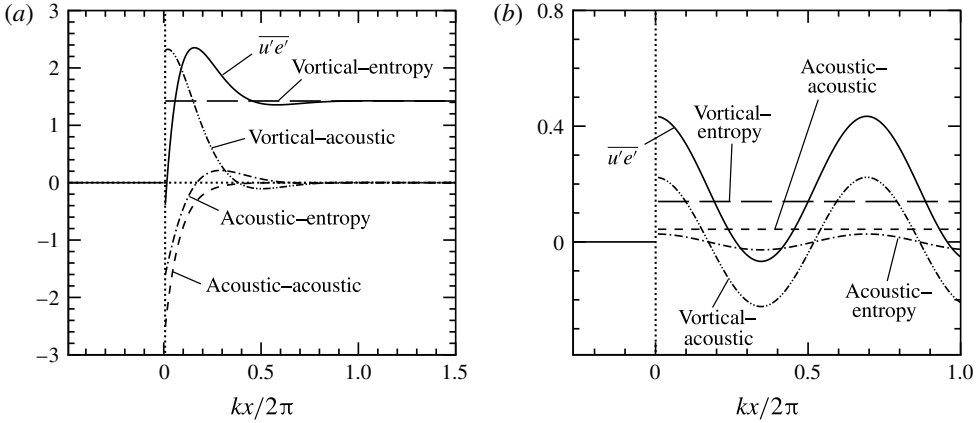
FIGURE 12. Modal decomposition of $\overline{u_2' e_2'}$ for the case of $M_1 = 2$. (a) $\psi = 75°$ (decaying regime) and (b) $\psi = 45°$ (propagating regime). Normalization is as described in figure 5.

the correlation gets statistically cancelled in the far field for a collection of waves representing a turbulence field.

The far-field results are qualitatively similar to the near-field energy flux plotted in figure 7(a). Peak negative values of the turbulent energy flux are obtained in the vicinity of the ψ_c curve, but the correlation is lower in magnitude than the corresponding near-field value. In the propagating regime, interactions with $\psi < \psi_z$ result in positive $\overline{u'e'}$ in the far field, similar to the near-field trend; the correlation magnitudes are once again smaller than the near-field levels. By comparison, high positive values of the far-field $\overline{u'e'}$ are obtained in the decaying regime, with the largest energy flux generated for interactions at 90° incidence for any given Mach number.

Figure 12 shows a Kovasznay mode decomposition of the energy flux correlation for a single-wave interaction with a Mach 2 shock wave. As per (2.4), the streamwise velocity u_2' has contributions from the acoustic and the vortical waves, and e_2' has contributions from the acoustic and the entropy waves. Thus, the energy flux correlation can be decomposed into four parts:

$$\overline{u_2' e_2'} = \left(\overline{u_2' e_2'}\right)_{aa} + \left(\overline{u_2' e_2'}\right)_{ae} + \left(\overline{u_2' e_2'}\right)_{va} + \left(\overline{u_2' e_2'}\right)_{ve}, \tag{3.8}$$

where subscripts aa, ae, va and ve correspond to acoustic–acoustic, acoustic–entropy, vortical–acoustic and vortical–entropy components, respectively, and they are given by

$$\left(\overline{u_2' e_2'}\right)_{aa} = \frac{1}{2\gamma}(\widetilde{F}\widetilde{K}^* + \widetilde{K}\widetilde{F}^*)\exp[\mathrm{i}(\widetilde{k} - \widetilde{k}^*)x], \tag{3.9a}$$

$$\left(\overline{u_2' e_2'}\right)_{ae} = \frac{-1}{2(\gamma - 1)}[\widetilde{F}\widetilde{Q}^* \exp[\mathrm{i}(\widetilde{k} - kr\cos\psi)x] + \widetilde{Q}\widetilde{F}^* \exp[\mathrm{i}(kr\cos\psi - \widetilde{k}^*)x]], \tag{3.9b}$$

$$\left(\overline{u_2' e_2'}\right)_{va} = \frac{1}{2\gamma}[\widetilde{K}\widetilde{G}^* \exp[\mathrm{i}(\widetilde{k} - kr\cos\psi)x] + \widetilde{G}\widetilde{K}^* \exp[\mathrm{i}(kr\cos\psi - \widetilde{k}^*)x]], \tag{3.9c}$$

$$\left(\overline{u_2' e_2'}\right)_{ve} = \frac{-1}{2(\gamma - 1)}\left[\widetilde{G}\widetilde{Q}^* + \widetilde{Q}\widetilde{G}^*\right]. \tag{3.9d}$$

The streamwise variation of the four components of the energy flux correlation is shown in figure 12(*a*) for the decaying interaction with $\psi = 75°$. The vortical–acoustic component takes high values just behind the shock, while the acoustic–entropy and acoustic–acoustic components of $\overline{u_2' e_2'}$ attain large negative values in the near field. All three components with a contribution from the acoustic mode decay to negligible values in the far field. By comparison, the vortical–entropy component takes a constant positive value in the downstream flow. The far-field energy flux correlation generated at the shock thus equals the non-zero vortical–entropy component. As earlier, the positive vortical–entropy contribution to $\overline{u_2' e_2'}$ implies energy transfer away from the shock, but a zero gradient in the streamwise direction suggests that there is no net build-up of internal energy due to this effect. On the other hand, the rapidly varying acoustic components of the turbulent energy flux can result in a local energy accumulation or depletion behind the shock wave.

The modal decomposition of the turbulent energy flux for a propagating interaction at $\psi = 45°$ is shown in figure 12(*b*). In this case, the vortical–entropy and the acoustic–acoustic components are both constant and positive in the downstream region. The sum of these two components yields the far-field value of $\overline{u_2' e_2'}$. The vortical–acoustic and acoustic–entropy components exhibit a sinusoidal variation about a zero mean, and therefore do not contribute to the far-field value. Note that the vortical–entropy component is the dominant contributor to the far-field energy flux; its value is substantially lower in this case than that in the interaction at $\psi = 75°$.

4. Three-dimensional isotropic spectrum

An expression for the downstream $\overline{u_2' e_2'}$ for a three-dimensional isotropic spectrum of planar waves can be written as

$$(\overline{u_2' e_2'})_{3D} = 4\pi \int_0^{\pi/2} \int_0^\infty (\overline{u_2' e_2'})_{2D} \, k^2 \sin \psi \, dk \, d\psi, \qquad (4.1)$$

where $(\overline{u_2' e_2'})_{2D}$ is the correlation obtained for a two-dimensional planar wave. Using (2.4), the above equation can be written as

$$(\overline{u_2' e_2'})_{3D} = 4\pi \int_0^{\pi/2} \int_0^\infty \left[\frac{\widetilde{Z}_1 + \widetilde{Z}_4}{2\gamma} - \frac{\widetilde{Z}_2 + \widetilde{Z}_3}{2(\gamma - 1)} \right] |A_v|^2 k^2 \sin \psi \, d\psi \, dk, \qquad (4.2)$$

where

$$\left.\begin{aligned}
\widetilde{Z}_1 &= (\widetilde{F}\widetilde{K}^* + \widetilde{F}^*\widetilde{K}) \exp[i(\widetilde{k} - \widetilde{k}^*)x], \\
\widetilde{Z}_2 &= \widetilde{G}\widetilde{Q}^* + \widetilde{G}^*\widetilde{Q}, \\
\widetilde{Z}_3 &= \widetilde{F}\widetilde{Q}^* \exp[i(\widetilde{k} - kr\cos\psi)x] + \widetilde{F}^*\widetilde{Q} \exp[-i(\widetilde{k}^* - kr\cos\psi)x], \\
\widetilde{Z}_4 &= \widetilde{G}\widetilde{K}^* \exp[-i(\widetilde{k}^* - kr\cos\psi)x] + \widetilde{G}^*\widetilde{K} \exp[i(\widetilde{k} - kr\cos\psi)x].
\end{aligned}\right\} \qquad (4.3)$$

The coefficients $\widetilde{F}$, $\widetilde{K}$, $\widetilde{G}$ and $\widetilde{Q}$ are functions of ψ, γ and M_1, and are independent of the wavenumber k and $\widetilde{k}$. The spatial inhomogeneity in the turbulent energy flux is therefore due to the exponential terms in the above expression. These represent either the sinusoidal variation of the energy flux correlation about the far-field mean value
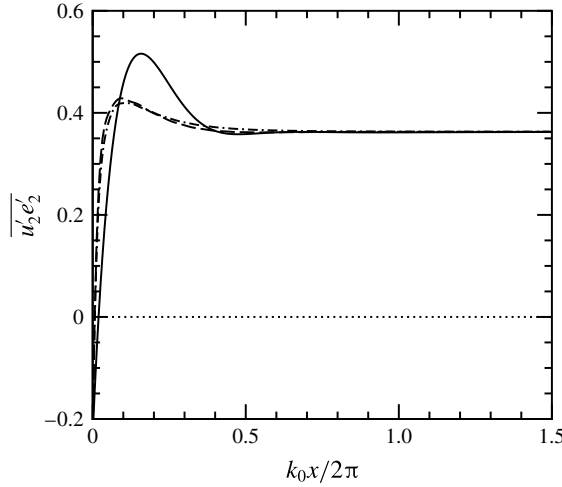
FIGURE 13. Turbulent energy flux along the streamwise direction for a three-dimensional isotropic spectrum of planar waves interacting with a shock of strength $M_1 = 2$ (spectrum 1: solid, spectrum 2: dashed, spectrum 3: dash-dotted). Normalization is as described in figure 5.

or an exponential decay behind the shock wave. At $x = 0$, the inhomogeneous parts drop out, such that the terms $\widetilde{Z}_1$, $\widetilde{Z}_2$, $\widetilde{Z}_3$ and $\widetilde{Z}_4$ are independent of the wavenumber and the integral can be split into two parts,

$$(\overline{u_2' e_2'})_{3D} = \int_0^{\pi/2} \left[\frac{1}{2\gamma}(\widetilde{Z}_1 + \widetilde{Z}_4) - \frac{1}{2(\gamma - 1)}(\widetilde{Z}_2 + \widetilde{Z}_3) \right] \sin \psi \, \mathrm{d}\psi \int_0^\infty E(k) \, \mathrm{d}k, \quad (4.4)$$

where the amplitude of the upstream velocity disturbance $|A_v|$ is written in terms of the three-dimensional energy spectrum $E(k)$ as

$$|A_v|^2 = \frac{E(k)}{4\pi k^2}. \quad (4.5)$$

The turbulent energy flux immediately behind the shock thus depends only on the integral of the energy spectrum, which is equivalent to twice the turbulence kinetic energy in the upstream flow. Further downstream, the inhomogeneous part of (4.2) decays exponentially with streamwise distance from the shock for $\psi > \psi_c$, i.e. plane wave interactions in the decaying regime. For interactions in the propagating regime ($\psi < \psi_c$), on the other hand, the integral of the inhomogeneous terms exhibits an algebraic decay away from the shock, as the constituent acoustic and vorticity/entropy waves travel at different speeds; see, for example, Griffond (2005). The far-field value of the energy flux correlation thus consists of only the homogeneous part, and is independent of the shape of the upstream spectrum specified in the problem. This is true for any second-order correlation, and is mentioned by Mahesh *et al.* (1995) for the turbulence kinetic energy generated by the interaction of a field of acoustic waves with a normal shock.

On the other hand, the peak positive turbulent energy flux generated by the shock is sensitive to the shape of the spectrum. Figure 13 shows the data computed using three
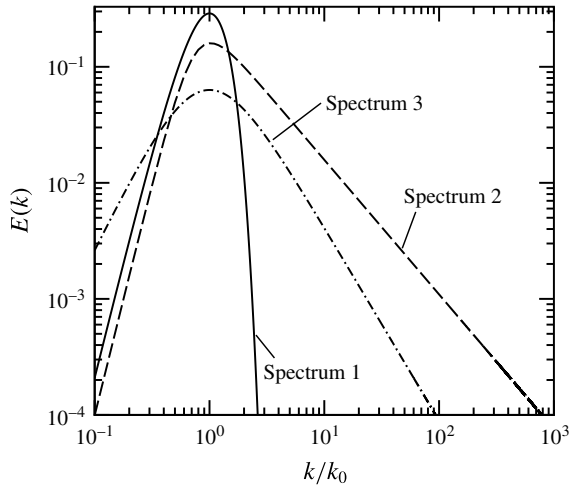
FIGURE 14. The energy distribution for varying wavenumbers shown for spectrum 1 (Mahesh *et al.* 1996), spectrum 2 (Larsson *et al.* 2013) and spectrum 3 (von Karman spectrum).

spectra, namely, a low-Reynolds-number spectrum taken from Mahesh *et al.* (1996),

$$\text{spectrum 1:} \quad E(k) \sim \left(\frac{k}{k_0} \right)^4 e^{-2(k/k_0)^2}, \tag{4.6}$$

the spectrum obtained from the DNS data of Larsson *et al.* (2013) at $Re_\lambda = 75$,

$$\text{spectrum 2:} \quad E(k) \sim \frac{(k/k_0)^4}{\left[(k/k_0)^4 + 0.32 \right]^{1.29}}, \tag{4.7}$$

and the von Karman spectrum (Pope 2000) given by

$$\text{spectrum 3:} \quad E(k) \sim \frac{(k/k_0)^2}{\left[(k/k_0)^2 + (5/6) \right]^{11/6}}, \tag{4.8}$$

where k_0 represents the wavenumber corresponding to the peak energy level. The shapes of the spectra are shown in figure 14, where the area under each curve is normalized to unity. The DNS spectrum is comparable to the von Karman spectrum in terms of its peak energy at $k_0 \sim 4$ and the energy at high wavenumbers. By comparison, the low-*Re* spectrum is devoid of high-wavenumber content.

The streamwise variations of the turbulent energy flux for Mach 2 are qualitatively similar for the three spectra. Spectrum 1 yields a higher peak energy flux, possibly because of higher energy over a limited range of wavenumbers, as compared to the other two spectra. The results for the von Karman spectrum are practically identical to those obtained using the DNS spectrum. It is therefore used for further analysis and comparison with the DNS data.

The three-dimensional near-field and far-field values of the turbulent energy flux are plotted as a function of the upstream Mach number in figure 15. The near-field values are positive at high Mach numbers, where the majority of the planar waves interacting
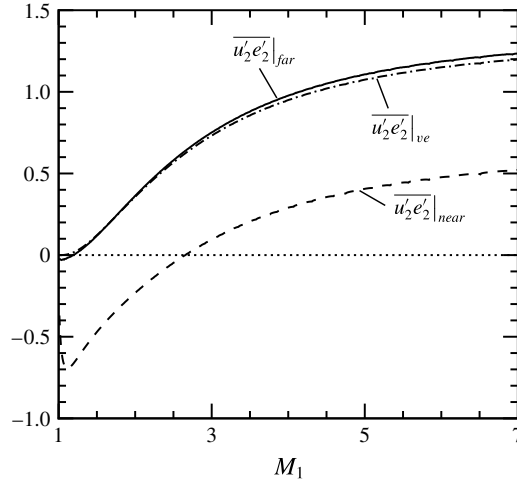
FIGURE 15. The near-field (dashed) and far-field (solid) $\overline{u_2'e_2'}$ for a three-dimensional isotropic spectrum for varying upstream Mach numbers. Also shown is the variation of the vortical–entropy component (dash dotted) of $\overline{u_2'e_2'}$. Normalization is as described in figure 5.

with the shock generate positive energy flux correlation. Only a small fraction of the waves, incident close to ψ_c, result in negative correlation (see figure 7*a*). For low Mach numbers, angles of incidence exceeding ψ_z result in negative energy flux behind the shock. The higher angles of incidence have a larger contribution to the spectrum integral due to the $\sin\psi$ factor in (4.1). The near-field turbulent energy flux computed for the three-dimensional spectrum, therefore, takes negative values for $M_1 < 2.7$. The correlation reaches its minimum value close to Mach 1, and vanishes in the limit $M_1 \to 1$, being physically consistent for interactions with very weak shock waves.

The far-field turbulent energy flux is positive except for a small range $1 < M_1 < 1.2$, and it is significantly higher than the near-field value for all Mach numbers. The far-field correlation is close to the three-dimensional vortical–entropy component plotted in figure 15. The contribution from the acoustic mode is negative, and it accounts for the difference between the far-field and near-field values of the correlation. Downstream of the shock, the acoustic components decay to negligible values within a distance of about one wavelength, corresponding to the most energetic wavenumber (see figure 16*a*). The variation of the three-dimensional turbulent energy flux with the streamwise distance shown here is qualitatively similar to the decaying single-wave interaction shown in figure 12(*a*). The transient peak, however, is less pronounced in the three-dimensional result, possibly because of averaging over a large number of planar wave interactions with different wavelengths.

Comparison of the streamwise variation of the turbulent energy flux at two Mach numbers (figure 16*a*,*b*) brings out some key differences. Immediately behind the shock, the acoustic components of the turbulent energy flux have large magnitude in the Mach 1.5 interactions, whereas the vortical–entropy component is dominant at Mach 3.5. The three acoustic terms give a net negative contribution to the energy flux, and their magnitudes are comparable at both the Mach numbers. On the other hand, the significantly higher positive vortical–entropy component at $M_1 = 3.5$ results in a positive near-field value of $\overline{u_2'e_2'}$. Also, note that the transient peak is absent in
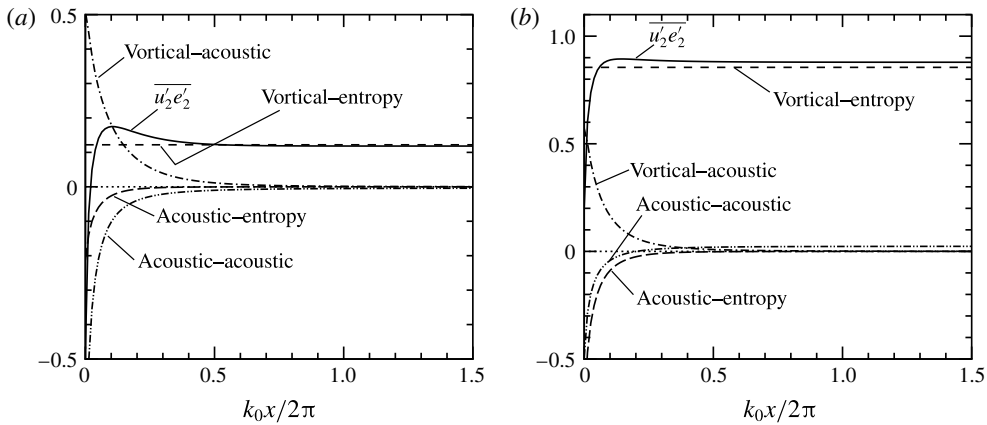
FIGURE 16. Variation of $\overline{u_2' e_2'}$ along the streamwise direction for a three-dimensional isotropic spectrum with upstream Mach number (*a*) $M_1 = 1.50$ and (*b*) $M_1 = 3.50$. Also shown are the four components of $\overline{u_2' e_2'}$ as per (3.8). Normalization is as described in figure 5.

the Mach 3.5 interaction, resulting in a monotonic rise from a low near-field value to the far-field asymptotic level. Further, there is a small non-zero acoustic–acoustic contribution to the turbulent energy flux at high Mach numbers, and it is reflected in the difference between the far-field value and the vortical–entropy component plotted in figure 15.

The three-dimensional results show some of the same physical trends observed in the single-wave interactions. These include the high gradient in $\overline{u' e'}$ in the acoustic-adjustment region behind the shock, which can cause a dip in the total energy. The mean energy conservation equation downstream of a steady one-dimensional shock wave can be written as

$$\overline{\rho}\, \overline{u} \frac{\partial \overline{E}}{\partial x} = \frac{\partial}{\partial x} \left(\overline{p}\, \overline{u} \right) - \gamma \frac{\partial}{\partial x} \left(\overline{\rho}\, \overline{u' e'} \right) + \text{other terms}, \tag{4.9}$$

neglecting the difference between Reynolds and Favre averaging. Here, $\overline{E}$ is the total mean energy of the gas (sum of the mean internal energy, the mean kinetic energy and the turbulence kinetic energy); $\overline{p}$, $\overline{u}$ and $\overline{\rho}$ are the mean pressure, velocity and density, respectively. A decrease in $\overline{u' e'}$ with distance from the shock can thus locally increase $\overline{E}$, and vice versa. A local peak in $\overline{u' e'}$ could imply a possible dip in the total energy of the flow, all other factors being constant. It is shown that the high-gradient and non-monotonic behaviour of the turbulent energy flux is due to the decay of the acoustic contributions in the energy flux correlation. The turbulence kinetic energy behind the shock also shows a similar qualitative behaviour, once again due to the decay of acoustic disturbances generated at the shock (Mahesh *et al.* 1997).

5. Comparison with DNS data

In this section, the theoretical LIA results obtained for the three-dimensional interaction are compared with the DNS data of Larsson *et al.* (2013). The cases considered are listed in table 1, and range from low supersonic Mach numbers to hypersonic values. The turbulent Mach number $M_t = \sqrt{R_{kk}}/\widetilde{a}$ and Re_λ are listed

M_1	M_t	Re_λ	δ/η	$R_{kk}/(2U_1^2)$	$k_0 L_\epsilon$	A_r	X
1.28	0.15	38	0.69	7.3×10^{-3}	3.9	0.030	3.8×10^{-3}
1.28	0.22	39	0.97	7.3×10^{-3}	3.9	0.042	7.6×10^{-3}
1.28	0.26	38	1.15	7.3×10^{-3}	4.0	0.051	1.1×10^{-2}
1.28	0.31	38	1.34	7.3×10^{-3}	3.8	0.057	1.6×10^{-2}
1.50	0.15	38	0.38	5.3×10^{-3}	3.9	0.036	3.8×10^{-3}
1.50	0.22	39	0.53	5.3×10^{-3}	4.3	0.048	6.9×10^{-3}
1.50	0.31	39	0.75	5.3×10^{-3}	4.1	0.066	1.6×10^{-2}
1.50	0.37	39	0.91	5.3×10^{-3}	4.2	0.079	2.4×10^{-2}
1.87	0.22	39	0.31	6.9×10^{-3}	3.8	0.059	6.7×10^{-3}
1.87	0.31	39	0.43	6.9×10^{-3}	4.0	0.082	1.5×10^{-2}
2.50	0.22	40	0.18	4.0×10^{-3}	4.3	0.083	7.0×10^{-3}
3.50	0.16	40	0.07	2.1×10^{-3}	4.1	0.080	3.5×10^{-3}
3.50	0.23	41	0.10	2.1×10^{-3}	4.3	0.111	6.4×10^{-3}
4.70	0.23	42	0.07	1.2×10^{-3}	4.3	0.138	6.4×10^{-3}
6.00	0.23	42	0.05	0.7×10^{-3}	4.4	0.193	7.5×10^{-3}
1.50	0.14	73	0.26	4.7×10^{-3}	3.0	0.032	2.1×10^{-3}
3.50	0.15	74	0.05	0.9×10^{-3}	2.9	0.076	2.0×10^{-3}

TABLE 1. The DNS cases from Larsson *et al.* (2013) used in the present study. The values correspond to the location immediately upstream of the mean shock wave. The ratio of shock thickness δ to Kolmogorov length scale η obtained by using (2.1) is given. The wavenumber k_0 associated with the peak energy is used to normalize the dissipation length scale L_ϵ. A_r (calculated using (B 5)) denotes the amplitude ratio of the upstream entropy wave and the upstream vorticity wave. X represents the ratio of the upstream turbulence kinetic energy associated with the acoustic fluctuations to the total turbulence kinetic energy present upstream of the shock.

for each interaction, where R_{kk} is twice the turbulence kinetic energy and $\widetilde{a}$ is the Favre-averaged speed of sound. Table 1 also lists the estimated ratio of the laminar shock thickness to the Kolmogorov scale δ/η, which was suggested by Ryu & Livescu (2014) to describe the deviation away from the ideal LIA limit. This ratio is less than 1.4 for all cases considered here, and much less than that for most cases. For this range of δ/η values, Ryu & Livescu (2014) found their DNS to operate in a regime converging towards the LIA result, but with some effects of either nonlinearity or (more plausibly) viscous decay behind the shock. The same conclusion was reached in Larsson *et al.* (2013), where the DNS cases used here were found to agree well with LIA, but with clear viscous effects. This sets the context for our comparison between LIA and DNS in this section.

Figure 17(*a*) compares the peak turbulent energy flux behind the shock wave obtained from LIA and DNS for a range of upstream Mach numbers. Note that the peak LIA value is identical to the asymptotic far-field $\overline{u_2' e_2'}$ for high Mach numbers. In accordance with the normalization employed for LIA, the energy flux correlation obtained from DNS is normalized by the upstream mean velocity U_1, the downstream mean temperature $\overline{T}_2$, the specific gas constant R and the turbulence kinetic energy just upstream of the shock wave. We compare the DNS data for the Favre-correlation $\widetilde{u'' e''}$ with the theoretical results for $\overline{u' e'}$ obtained from LIA. There is negligible difference between the two averaging procedures when computed using the DNS data sets.
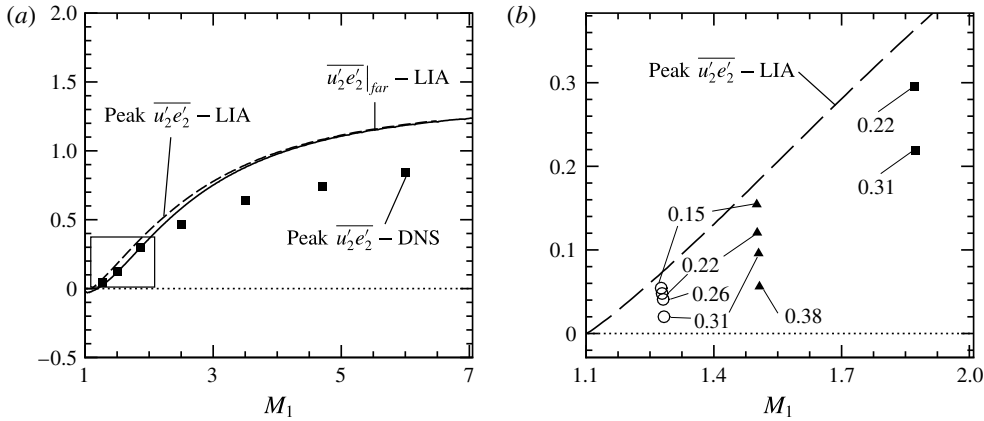
FIGURE 17. Variation of $\overline{u_2' e_2'}$ with upstream Mach number as per LIA (lines) and DNS (symbols). (*a*) DNS data correspond to $M_t = 0.22$ and $Re_\lambda = 40$. (*b*) Magnified view highlighting the effect of M_t on the peak DNS $\overline{u_2' e_2'}$ for three Mach numbers ($M_1 = 1.27$ (circle), 1.50 (gradient) and 1.87 (square)) at $Re_\lambda = 40$. Normalization is as described in figure 5.

The variation of the peak turbulent energy flux with Mach number follows identical trends in DNS and LIA. There is also a good quantitative match at low Mach numbers. All the DNS data plotted in the figure correspond to a value of $M_t = 0.22$, and the effect of varying upstream M_t on the postshock statistics is discussed subsequently. Both DNS and LIA yield a finite limiting value of the normalized turbulent energy flux at high Mach numbers, i.e.

$$\lim_{M_1 \to \infty} \overline{u_2' e_2'} = \text{const.}, \qquad (5.1)$$

which implies that the dimensional turbulent energy flux is proportional to the upstream mean velocity and the postshock mean temperature. The asymptotic value of the turbulent energy flux at high Mach number therefore scales as M_1^3 for a fixed upstream temperature $\overline{T}_1$ (as $U_1 = M_1 \sqrt{\gamma R T_1}$ and $\overline{T}_2 / \overline{T}_1 \propto M_1^2$ for $M_1 \to \infty$). This is consistent with the linear inviscid formulation of LIA, where the temperature fluctuations T_2' are proportional to the mean temperature $\overline{T}_2$ and all velocity fluctuations, including u_2', scale with U_1. Thus, the peak turbulent energy flux obtained from DNS follows a high-Mach-number scaling as per the linear inviscid framework. The data are, however, about 25 % lower in magnitude than the LIA prediction.

Figure 17(*b*) shows the effect of turbulent Mach number M_t on the peak values of the energy flux behind the shock wave. The DNS peak turbulent energy flux approaches the LIA prediction as the upstream turbulence intensity decreases for three upstream Mach numbers, $M_1 = 1.28$, 1.5 and 1.87. A similar trend is also observed at $M_1 = 3.5$ (data not shown). This is in consonance with the results presented by Ryu & Livescu (2014), where postshock (streamwise and transverse) Reynolds stresses are found to match LIA results in the limit of $M_t \to 0$, even at low Reynolds numbers.

We next compare the streamwise variation of the turbulent energy flux obtained from DNS and LIA in figure 18. The Mach number of the interaction is 1.5 and DNS data corresponding to two Reynolds numbers are used for comparison. The shock is
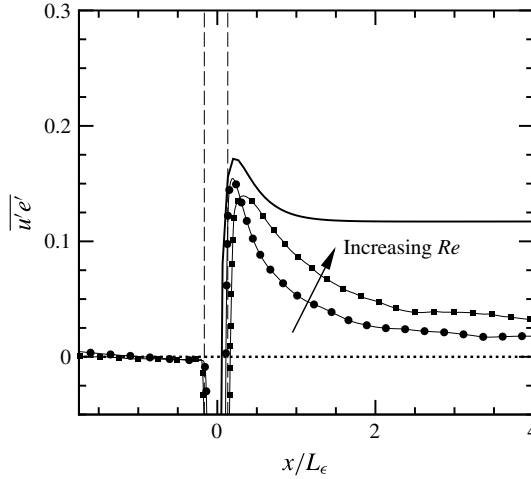
FIGURE 18. Streamwise variation of the turbulent energy flux for $M_1 = 1.50$ from LIA (lines) and $(M_1, M_t) = (1.50, 0.15)$ from DNS (lines with symbols). The effect of Reynolds number is also shown with $Re_\lambda = 40$ (circle) and $Re_\lambda = 75$ (square). $x = 0$ represents the center of the mean shock thickness, and the vertical lines near $x = 0$ represent the region of mean shock thickness. Normalization is as described in figure 5.

located at $x = 0$ with the two vertical lines representing the region of DNS unsteady shock movement. The streamwise distance is normalized by the dissipation length scale L_ϵ, calculated just upstream of the shock as

$$L_\epsilon = (R_{kk}/2)^{3/2}/\epsilon, \tag{5.2}$$

where ϵ is the turbulence dissipation rate, and the values of $k_0 L_\epsilon$ are listed in table 1. In the absence of viscous dissipation in the linear theory, the most energetic wavenumber (k_0) in the upstream turbulence is used to obtain the characteristic length. It is converted to an equivalent dissipation length scale for LIA using the value of $k_0 L_\epsilon \approx 3$–4 obtained in the DNS study (Larsson *et al.* 2013).

DNS data at both $Re_\lambda = 40$ and 75 have large negative values of the turbulent energy flux in the region of the unsteady shock wave. Starting from negative values at the shock, the energy flux correlation increases to peak positive values just behind the shock. The DNS trend is thus qualitatively similar to the variation of the energy flux obtained from the linear theory. This, along with the comparison of the peak values described earlier, indicates that LIA is possibly capturing some of the key physical processes involved in the generation of turbulent energy flux at the shock wave. Following the positive peak, the DNS energy flux reduces to low values away from the shock that are far below the far-field asymptotic $\overline{u'e'}$ predicted by the linear inviscid theory. This is because of the fact that LIA is based on inviscid approximations, while there are considerable viscous effects in the DNS computations performed at relatively low Reynolds numbers. Increasing the Reynolds number in the DNS, however, results in the data approaching the LIA predictions that are representative of the limit of infinite Reynolds number.

The case with higher Reynolds number has a slight dip in the peak positive $\overline{u'e'}$ as compared to the corresponding value for lower Reynolds number. This could be attributed to the fact that the $Re_\lambda = 75$ case has a broader spectrum than the simulation

at lower Reynolds number. Reduction of the peak energy flux for a spectrum with energy distributed over a wider range of scales has been reported in figure 13. We also note that the streamwise locations of the peak turbulent energy flux for the two Reynolds numbers are close to each other, when normalized by the dissipation length scale. This is not the case when the Kolmogorov length scale is used for normalization. The close match in the value of the peak energy flux as well as its location for the two different Reynolds numbers highlights the fact that the near-field energy flux is governed by large-scale inviscid processes. We further investigate the physical mechanisms responsible for the postshock $\overline{u'e'}$ variation by studying the budget of its transport equation in §5.2.

It is interesting to note that the peak energy flux values are obtained not at the shock, but in the acoustic adjustment region behind the shock wave. Conventional models based on the gradient hypothesis are insensitive to this phenomenon, and respond only to the shock gradient. Outside the shock wave, they switch to the local temperature gradient in the downstream flow. The results reported here show that this may be grossly inadequate, as the primary effect of the shock wave on heat transfer is via the peak turbulent energy flux following the shock wave. This region scales with the integral length scale of the disturbance field, representative of the large-scale turbulent motion. It may therefore be important to predict this phenomenon in realistic flows. Most conventional models are based on a local formulation for the turbulent heat flux vector, with no downstream influence of the shock wave. A few advanced models based on transport equations for the energy flux correlation and related quantities (Xiao *et al.* 2007) may be able to introduce this effect.

5.1. *Effect of upstream thermodynamic fluctuations*

The LIA model used here assumes a purely vortical incoming turbulence field, but the more realistic situation (both in canonical DNS and in realistic flows) is to have a mixture of vortical, acoustic and entropy fluctuations. The purpose of this section is to roughly estimate the importance of these additional effects.

5.1.1. *Upstream entropy mode*

Larsson & Lele (2009) report small but finite pressure, temperature and density fluctuations upstream of the shock, with magnitudes

$$\frac{\rho'_{rms}}{\overline{\rho}_1 M_t^2} = 0.44 \pm 0.01, \qquad \frac{p'_{rms}}{\gamma \overline{p}_1 M_t^2} = 0.39 \pm 0.02, \qquad \frac{T'_{rms}}{(\gamma - 1)\overline{T}_1 M_t^2} = 0.38 \pm 0.02,$$

(5.3a−c)

for the majority of the cases listed in table 1. The entropy fluctuations in the DNS are found to be of magnitude

$$\frac{s'_{rms}}{c_p M_t^2} = 0.1 \pm 0.01,$$ (5.4)

where c_p is the specific heat at constant pressure. Entropy fluctuations are modeled in the linearized density field in LIA, and thus we use the amplitude $\rho'_{rms,\text{LIA}} = s'_{rms}\overline{\rho}_1/c_p$ to model the entropy fluctuations in the LIA (with details given in appendix B). While the phase difference between the vortical and entropy modes could be extracted from DNS, in this particular flow configuration that phase difference has no physical meaning and is solely an artefact of the inflow condition. However, in many realistic
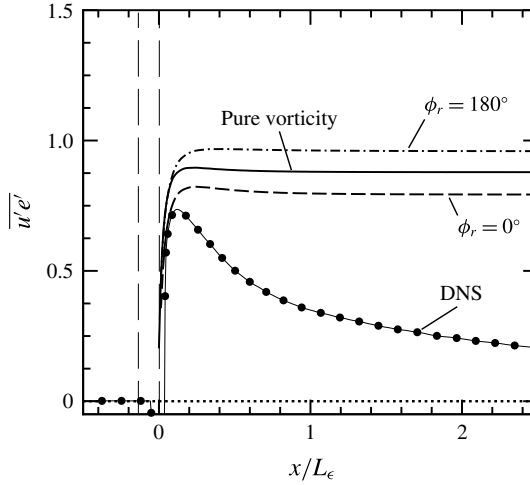
FIGURE 19. Streamwise variation of turbulent energy flux for $M_1 = 3.50$ from LIA (solid line), LIA with added upstream entropy fluctuations with $\phi_r = 0°$ and $\phi_r = 180°$ (dashed lines) and DNS (line with symbols) at $(M_1, M_t, Re_\lambda) = (3.50, 0.16, 40)$. The amplitude ratio A_r for the upstream entropy case is provided in table 1. $x = 0$ represents the center of the mean shock thickness, and the vertical lines near $x = 0$ represent the region of mean shock thickness. Normalization is as described in figure 5.

flows, most notably in boundary layers, there is a specific favored correlation between these modes. In light of this, we consider a whole range of phase angles and focus on the bounding cases.

In figure 19, we compare the streamwise turbulent energy flux generated from a pure vorticity interaction with a case having finite upstream entropy fluctuations. The results are for $M_1 = 3.50$, and two cases of upstream entropy fluctuations are considered, with phase angle $\phi_r = 0°$ and $180°$, for the same amplitude. Other angles have also been studied to confirm that the above two values of ϕ_r are the extreme bounds. The figure also shows the DNS data for $M_1 = 3.5$, $M_t = 0.16$ and $Re_\lambda = 40$. A value of $\phi_r = 0$ corresponds to a negative correlation between the velocity and energy fluctuations upstream of the shock. Such an upstream correlation yields a value of the downstream turbulent energy flux that is closer to the DNS data. For this ϕ_r, an increase in the amplitude ratio A_r (increase in the relative magnitude of the upstream entropy wave) further reduces the value of the turbulent energy flux. Upstream velocity and energy fluctuations that are in phase ($\phi_r = 180°$) have an amplifying effect on the turbulent energy flux correlation; a similar amplification is observed for the downstream energy variance as well (data not shown here) when $\phi_r = 180°$. The case shown here is for a single Mach number but the trends are similar for other Mach numbers as well.

5.1.2. *Upstream acoustic mode*

The acoustic and vorticity modes upstream of the shock travel at different speeds and are not correlated to each other. Therefore, the turbulent energy flux generated by a combined field of acoustic and vorticity modes can be studied by first analysing the independent interaction of acoustic waves with the shock. The procedure is similar to that of vorticity waves interacting with the shock and is given elaborately in Moore (1954) and Mahesh *et al.* (1996). The necessary details are provided in appendix C.
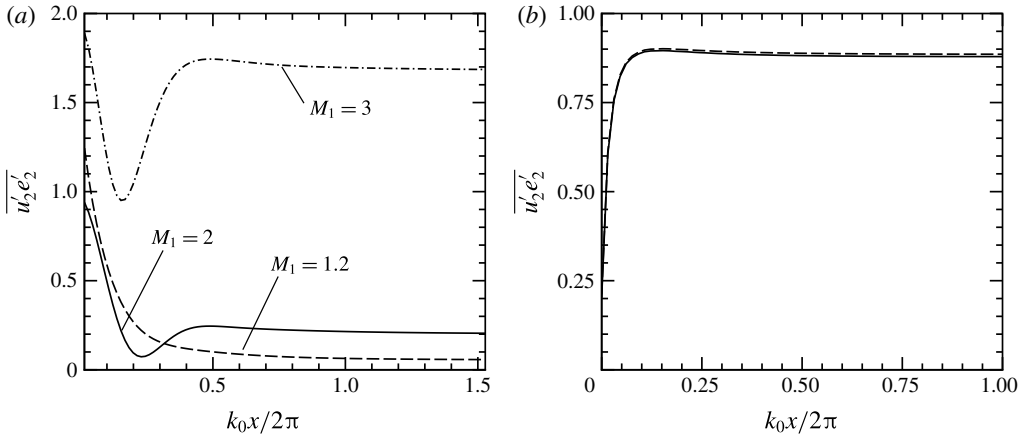
FIGURE 20. LIA results for streamwise variation of the turbulent energy flux with upstream disturbance field as (*a*) purely acoustic fluctuations, (*b*) purely vortical (solid) and combined acoustic/vortical (dashed) at $M_1 = 3.50$, where the relative amplitude of the acoustic field is the estimated upper bound for the DNS case at $(M_t, Re_\lambda) = (0.16, 40)$. Normalization is as described in figure 5.

Figure 20(*a*) plots the streamwise variation of the shock-normal turbulent energy flux when a purely acoustic field interacts with a shock wave (located at $x = 0$). The turbulent energy flux is normalized by the upstream turbulence kinetic energy of the acoustic disturbances, and the streamwise distance is normalized using the most energetic wavenumber k_0 in the upstream turbulence. We see a monotonic decay in the energy flux correlation at low Mach numbers ($M_1 = 1.2$), and a non-monotonic variation for higher Mach numbers. Similar behaviour was reported by Mahesh *et al.* (1995) in the streamwise variation of downstream TKE for the pure acoustic interaction. As earlier, the rapid variation in the turbulent energy flux near the shock can be attributed to the decaying acoustic waves generated at the shock wave. The far-field value of the correlation is largely due to the entropy and vorticity modes, and its magnitude increases upon increasing the upstream Mach number. The normalized turbulent energy flux is found to be of order 1 in the near field, and is comparable in magnitude to that in the case of vorticity waves interacting with a shock (figure 16).

The turbulent energy flux generated by the combined interaction of the vortical and acoustic fields is given by

$$\frac{\overline{u_2' e_2'}}{\text{TKE}_{total}} = \frac{\overline{u_2' e_2'}_{vort} + \overline{u_2' e_2'}_{ac}}{\text{TKE}_{vort} + \text{TKE}_{ac}}, \tag{5.5}$$

where subscript *vort* is associated with the correlations obtained from the pure vortical interaction, and subscript *ac* corresponds to the pure acoustic interaction, both studied independently. The above equation can be written as

$$\frac{\overline{u_2' e_2'}}{\text{TKE}_{total}} = (1 - X) \frac{\overline{u_2' e_2'}_{vort}}{\text{TKE}_{vort}} + X \frac{\overline{u_2' e_2'}_{ac}}{\text{TKE}_{ac}}, \tag{5.6}$$

where X represents the ratio of dilatational turbulence kinetic energy associated with the acoustic mode to the total turbulence kinetic energy in the combined vortical–acoustic turbulence. This is similar to the form used by Mahesh *et al.* (1995) to study

the effect of a combined field of vorticity and acoustic disturbances on the TKE evolution behind a shock wave.

It is not trivial to extract the value of X from the DNS data, since a Helmholtz decomposition is complicated by the non-periodic shock-normal direction. An upper bound on X can be found by assuming that the upstream pressure fluctuations have contributions solely from the acoustic mode, for which (Mahesh *et al.* 1995)

$$\frac{\text{TKE}_{ac}}{U_1^2} = \frac{1}{2} \left(\frac{1}{\gamma M_1}\right)^2 \frac{\overline{p_1'^2}}{\overline{p}_1^2}, \tag{5.7}$$

where the pressure variance $\overline{p_1'^2}$ just before the shock is taken from the DNS data, as per (5.3). Since the pressure fluctuations in reality also have a hydrodynamic contribution (the pseudo-sound, from the vortical fluctuations; see Ristorcelli & Blaisdell (1997)), this formula clearly overestimates TKE_{ac}. For the DNS cases in this study, we find the bound $X \lesssim 10^{-3}$ to 10^{-2} as given in table 1.

Figure 20(b) shows the streamwise variation of the turbulent energy flux values when the upstream turbulence has a combination of vortical and acoustic disturbances. The results correspond to a Mach number of 3.5, and the combined interaction results are obtained by using (5.6). The turbulent Mach number is 0.16 and it gives a value of $X = 3.5 \times 10^{-3}$. The turbulent energy flux obtained for the combined interaction is almost identical to that for the purely vortical disturbances upstream of the shock wave. The upstream acoustic mode has negligible effect, and this is primarily because of the low value of the ratio of dilatational to total turbulence kinetic energy. This may not be the case for flows with a significant acoustic mode contribution, i.e. dilatational velocity field, upstream of the shock. Examples include turbulent free shear layers and their interaction with shock waves, in practical applications like underexpanded jets.

Furthermore, high-speed boundary layers are known to have significant entropy fluctuations in addition to a vortical disturbance field. As per Morkovin's hypothesis, the ratio of temperature to velocity fluctuations scales as the square of the mean flow Mach number. The sign of the velocity–temperature correlation is also known to strongly influence shock–turbulence interaction (Veera & Sinha 2009). Negative correlation yields higher TKE amplification at the shock compared to that in the case of positively correlated vorticity–entropy disturbances in the upstream flow (Mahesh *et al.* 1997). Velocity and temperature fluctuations in high-speed boundary layers are usually negatively correlated, but the correlation may be positive for highly cooled walls. These can have a significant effect on the turbulent energy flux generated by a shock wave. The presence of mean shear and shock curvature in realistic flows can introduce additional effects not considered in this work.

5.2. *Transport equation for turbulent energy flux*

We next investigate the physical processes that influence the turbulent energy flux behind a shock wave by computing the budget of its transport equation. We start with the instantaneous momentum and energy conservation equations given by

$$\frac{\partial}{\partial t}(\rho u_i) + \frac{\partial}{\partial x_j}(\rho u_i u_j) = -\frac{\partial p}{\partial x_i} + \frac{\partial \tau_{ij}}{\partial x_j}, \tag{5.8}$$

$$\frac{\partial}{\partial t}(\rho e) + \frac{\partial}{\partial x_j}(\rho e u_j) = -p\frac{\partial u_i}{\partial x_i} - \frac{\partial q_j}{\partial x_j} + \tau_{ij}\frac{\partial u_i}{\partial x_j}, \tag{5.9}$$

where τ_{ij} is the viscous stress tensor and q_j is the heat conduction flux given by $q_j = -\kappa \partial T/\partial x_j$, κ being the conductivity of the fluid. In this section, for the sake of brevity, we use tensor notation to denote the terms. Subscripts 1, 2 and 3, wherever applicable, correspond to x, y and z directions, respectively. The first and second terms on the right-hand side of (5.9) represent the pressure–dilatation and conduction mechanisms, while the third term represents viscous dissipation. A moment of (5.8) with e'' can be added to a moment of (5.9) with u'' and then Reynolds-averaged to yield a transport equation for $\overline{\rho u'' e''}$. Details are provided in Hanifi *et al.* (1999).

For the canonical case under consideration, $\partial \bar{f}/\partial y = \partial \bar{f}/\partial z = 0$, where $\bar{f}$ is any mean quantity. The gradient of the mean quantity along the streamwise direction is negligible away from the shock, i.e. $\partial \bar{f}/\partial x \approx 0$. Also, the averaged turbulent statistics are steady and one-dimensional, which yields $\partial \bar{g}/\partial t = \partial \bar{g}/\partial y = \partial \bar{g}/\partial z = 0$ for any turbulent correlation $\bar{g}$. The governing equation for the streamwise energy flux thus reduces to

$$\overline{\rho}\widetilde{u}\frac{\partial}{\partial x}\widetilde{u''e''} = \underbrace{\overline{e''\frac{\partial \tau_{1j}}{\partial x_j}}}_{\substack{\text{Vis. diffusion} \\ \text{and dissipation}}} - \underbrace{\overline{e''\frac{\partial p}{\partial x}}}_{\substack{\text{Press.–energy}}} - \underbrace{\overline{pu''\frac{\partial u''_j}{\partial x_j}}}_{\substack{\text{Pressure–dilatation.}}} - \underbrace{\overline{u''\frac{\partial q_j}{\partial x_j}}}_{\substack{\text{Conduction}}}$$

$$+ \underbrace{\overline{u''\tau_{jk}\frac{\partial u''_j}{\partial x_k}}}_{\substack{\text{Vis. dissipation}}} - \underbrace{\frac{\partial}{\partial x}\overline{\rho e''u''u''}}_{\substack{\text{Turbulent transp.}}} \ . \tag{5.10}$$

The first two terms on the right-hand side are the correlation of the viscous stress and the pressure gradient with internal energy fluctuation. The former represents the viscous diffusion and dissipation mechanism, while the latter corresponds to the pressure–energy effect. The third, fourth and fifth terms are correlation of pressure–dilatation, heat conduction and viscous dissipation with the streamwise velocity fluctuation. The last term represents the turbulent transport of the energy flux correlation.

5.2.1. *Budget using DNS data*

The budget of the above transport equation is computed for the case of $(M_1, M_t, Re_\lambda) = (1.5, 0.15, 40)$, and the data are presented in figure 21(*a*). A total of 120 flow-field realizations at different instants of time are used to compute the time-averaged turbulence statistics, and statistical convergence is checked for. It is found that the pressure–energy and pressure–dilatation terms identified in (5.10) are the major contributors to the evolution of $\widetilde{u''e''}$. The viscous diffusion and dissipation terms, as well as the conduction and turbulent transport terms, are comparatively negligible, and are not shown in the figure. The difference between the left- and right-hand sides of the transport equation is shown as an error in figure 21 (thin solid line around zero). It has a negligible value outside the region of mean shock thickness where the DNS results are compared with linear theory.

The pressure–energy term has a peak positive contribution close to the shock and drops to low values in the far field. The pressure–dilatation term also has a peak positive contribution at the shock; it attains a minimum (negative) value behind the shock before decaying to zero. The convection term (left-hand side) in (5.10) is a resultant of the pressure–energy and pressure–dilatation contributions. It takes a positive value in the near field, which corresponds to a rapid increase in the energy
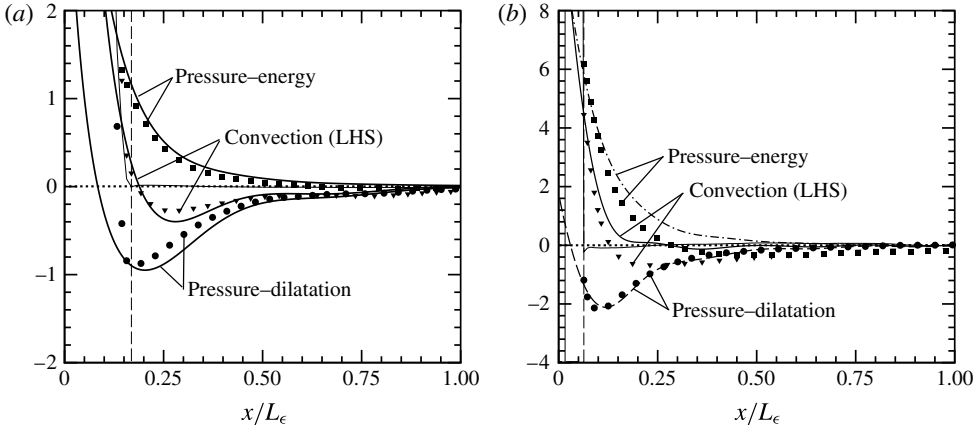
FIGURE 21. Budget of the transport equation for the turbulent energy flux from DNS data (symbols) and LIA (lines) corresponding to (*a*) (M_1, M_t, Re_λ) = (1.5, 0.15, 40) and (*b*) (M_1, M_t, Re_λ) = (3.5, 0.15, 40). The vertical line near $x/L_\epsilon = 0$ (dashed) represents the end of the region of mean shock thickness. The error in the DNS budget is also shown (thin solid line around zero). Normalization is as described in figure 5.

flux behind the shock. The zero-crossing of the term on the left-hand side corresponds to the peak positive $\overline{u_2'e_2'}$. Subsequent negative values of the convection term indicate a decay of the correlation to low levels in the far field.

The pressure–dilatation term in the energy conservation equation (5.9) represents the work done by pressure forces in compressing/expanding the gas. A locally high pressure associated with negative dilatation, such that $p(\partial u_i''/\partial x_i) < 0$, increases internal energy. How this increase in the energy is transferred by turbulent velocity fluctuations is governed by the term $\overline{pu''(\partial u_j''/\partial x_j)}$ in the turbulent energy flux equation (5.10). The fact that the correlation is negative implies that the internal energy fluctuations generated by the pressure–dilatation work are convected, on average, in the negative *x*-direction. It therefore contributes as a negative source term in the transport equation for turbulent energy flux. The pressure–dilatation term can be split into two parts based on the mean and the fluctuating pressure as

$$\overline{pu''\frac{\partial u_j''}{\partial x_j}} = \overline{\bar{p}u''\frac{\partial u_j''}{\partial x_j}} + \overline{p'u''\frac{\partial u_j''}{\partial x_j}}. \tag{5.11}$$

The major contribution to the budget is from the first part, which is proportional to the mean pressure downstream of the shock. The second part, involving a higher-order correlation, is comparatively small in magnitude. The pressure–dilatation effect on the turbulent energy flux is therefore determined primarily by the correlation $\overline{u''(\partial u_j''/\partial x_j)}$. The data show that positive velocity fluctuations are associated with local expansion of the fluid element. Similarly, lower streamwise velocity is statistically correlated with locally compressed fluid. The correlation $\overline{u''(\partial u_j''/\partial x_j)}$ can be expanded as

$$\overline{u''\frac{\partial u_j''}{\partial x_j}} = \frac{\partial}{\partial x}\frac{\overline{u''^2}}{2} + \overline{u''\frac{\partial v''}{\partial y}} + \overline{u''\frac{\partial w''}{\partial x}}, \tag{5.12}$$

where the first term on the right-hand side can be argued to be positive in the acoustic-adjustment region behind the shock. It represents the build-up of streamwise Reynolds stress as a result of the acoustic decay, and can be seen clearly in figure 5(*b*).

The physics behind the pressure–energy term in (5.10) can be elucidated as follows. A pressure gradient in a flow can accelerate or decelerate a fluid element. A locally negative pressure gradient would generate positive streamwise velocity fluctuations, all other factors being constant. This, when correlated with locally high internal energy ($e'' > 0$), would contribute to a positive turbulent energy flux. The region ($0 < x/L_\epsilon < 1$) considered for the budget calculation is dominated by the acoustic mode. The thermodynamic fluctuations can therefore be assumed to be approximately isentropic, i.e., $p'/(\gamma \bar{p}) \simeq T'/((\gamma - 1)\overline{T})$, such that the pressure–energy term can be written as

$$-\overline{e'' \frac{\partial p'}{\partial x}} = -c_v \overline{T' \frac{\partial p'}{\partial x}} = -\frac{1}{\gamma \bar{\rho}} \frac{\partial}{\partial x} \left(\overline{\frac{p'^2}{2}} \right), \qquad (5.13)$$

once again neglecting the differences between Favre and Reynolds averaging. Large pressure fluctuations are generated by interactions at high angles of incidence. In the decaying regime, the pressure variance decreases exponentially to small values within one integral length scale. The pressure–energy source term shows identical trends, suggesting that it is dominated by the acoustic mode.

5.2.2. *Linear inviscid approximations*

A transport equation for the turbulent energy flux in the linear inviscid framework can be derived from the linearized Euler equations given by

$$\left. \begin{array}{l} \dfrac{\partial u'}{\partial t} + \bar{u} \dfrac{\partial u'}{\partial x} = -\dfrac{1}{\bar{\rho}} \dfrac{\partial p'}{\partial x}, \\[3mm] \dfrac{\partial e'}{\partial t} + \bar{u} \dfrac{\partial e'}{\partial x} = -\dfrac{\bar{p}}{\bar{\rho}} \left(\dfrac{\partial u'_j}{\partial x_j} \right), \end{array} \right\} \qquad (5.14)$$

where the viscous and conduction effects have been neglected in line with the LIA assumptions, and the higher-order terms are also assumed to be small. A transport equation for the turbulent energy flux can be derived from the above equations using the steps outlined earlier for the derivation of (5.10):

$$\bar{\rho} \, \bar{u} \frac{\partial}{\partial x} \overline{u'e'} = - \underbrace{\overline{e' \frac{\partial p'}{\partial x}}}_{\text{Press.–energy}} - \underbrace{\overline{\bar{p} u' \frac{\partial u'_j}{\partial x_j}}}_{\text{Pressure–dilatation}}. \qquad (5.15)$$

The two terms on the right-hand side are the pressure–energy and pressure–dilatation terms, which are almost identical to their counterparts in (5.10). Again, the differences due to Favre and Reynolds fluctuations are found to be minimal from the DNS data. The viscous, conduction and turbulent transport terms seen in (5.10) are absent here due to the linear inviscid assumptions.

Using LIA, we plot the budget of (5.15) in figure 21(*a*) for the region downstream of the shock corresponding to the case of $M_1 = 1.5$. We use the von Karman spectrum (4.8) to compute the budget. We observe no substantial difference when the DNS spectrum (4.7) is used instead. There is a good qualitative as well as quantitative match with DNS. The pressure–energy term shows a similar variation to its DNS

counterpart, assuming a high positive value just behind the shock and monotonically decreasing to negligible levels downstream. The dilatation term from LIA also shows a trend similar to that observed in the DNS data, with a slightly higher negative peak. As a result, the convective term (left-hand side) has a more pronounced negative peak in LIA than in DNS.

The budget of the $\overline{u'e'}$ transport equation for Mach 3.5 (in figure 21b) shows the same qualitative trends as the budget for the lower Mach number. The magnitude of the terms, however, is significantly larger and they lead to a higher postshock turbulent energy flux. We also find that the convection and pressure–energy terms in DNS take identical negative values beyond $x/L_\epsilon = 0.5$, while the pressure–dilatation term is close to zero. The LIA data match the DNS pressure–dilatation term closely. The linear theory also reproduces the qualitative trends observed in the DNS budget, except for the convection term. The DNS data show a prominent zero-crossing of the left-hand side, which corresponds to the peak $\overline{u'e'}$ at $x/L_\epsilon \simeq 0.12$. The LIA prediction for this case has no noticeable peak in the postshock energy flux profile, as noted earlier. The trends in the DNS budget shown in figure 21 continue further downstream up to $x/L_\epsilon \sim 2$, beyond which budget data are not available. In particular, the pressure–energy and pressure–dilatation terms have dominant contributions, although with lower magnitudes than those in the figure, and the viscous diffusion/dissipation as well as the conduction terms are relatively small.

5.3. *Integrated budget*

The cumulative contribution of each of the mechanisms to the value of the turbulent energy flux in the region downstream of the shock can be found by integrating the transport equation, as carried out for Reynolds stresses in Larsson *et al.* (2013). The integrated form of (5.10) can be written as

$$\left(\widetilde{u_2'' e_2''}\right)_x = \left(\widetilde{u_2'' e_2''}\right)_{\varsigma=x^*} + \frac{1}{\overline{\rho}\widetilde{u}} \left[\int_{\varsigma=x^*}^x (\text{Press.--energy}) \, \mathrm{d}\varsigma + \int_{\varsigma=x^*}^x (\text{Press.--dil.}) \, \mathrm{d}\varsigma \right]$$

$$+ \frac{1}{\overline{\rho}\widetilde{u}} \left[\int_{\varsigma=x^*}^x (\text{Remainder}) \, \mathrm{d}\varsigma \right]. \tag{5.16}$$

Here, $\varsigma = x^*$ indicates the point where the mean shock thickness ends (the vertical line at $x/L_\epsilon = 0.16$ and 0.06 in figure 21a,b). The remainder in the above equation represents the terms that make relatively smaller contributions to the budget, for example the viscous dissipation and conduction terms. The budget of (5.16) computed using the DNS data is plotted in figure 22 (symbols) for Mach 1.5 and Mach 3.5. A similar integrated budget of (5.15) computed using LIA for the two Mach numbers is shown for comparison (lines).

The pressure–dilatation term has a negative cumulative effect and it saturates to a constant level due to the vanishingly small magnitude of the source term away from the shock. There is a fairly good match between the LIA and DNS values of the integrated pressure–dilatation term at both Mach numbers. On the other hand, the pressure–energy term has a positive cumulative contribution, with DNS assuming a lower value than the corresponding LIA result. The integrated effect reaches a peak value behind the shock and decreases further downstream, indicating that the pressure–energy term is negative in the far field. The slope of the integrated pressure–energy term matches the decay rate of the DNS turbulent energy flux away from the shock. This trend is more prominent at the higher Mach number,
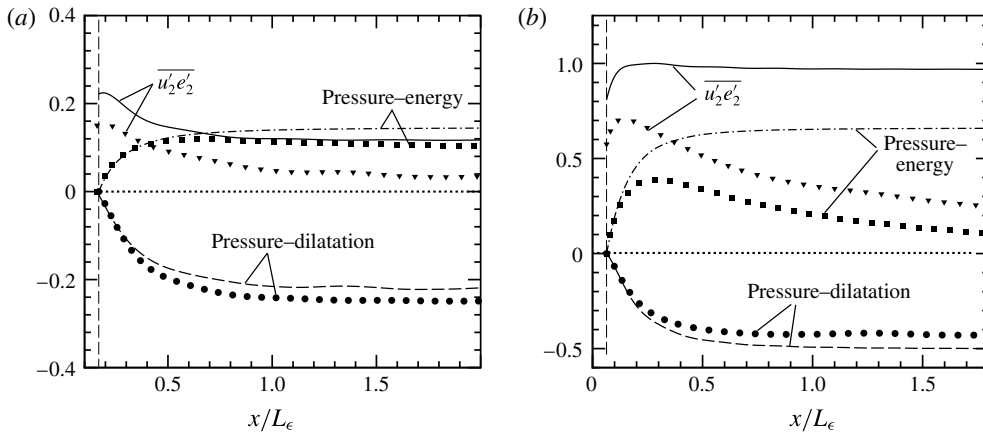
FIGURE 22. Integrated budget of the transport equation for the turbulent energy flux from DNS (symbols) and LIA (lines) corresponding to (*a*) $(M_1, M_t, Re_\lambda) = (1.5, 0.15, 40)$ and (*b*) $(M_1, M_t, Re_\lambda) = (3.5, 0.15, 40)$. The vertical line at $x/L = 0$ (dashed) represents the end of the mean shock thickness. Normalization is as described in figure 5.

and implies that the pressure–energy mechanism is primarily responsible for the discrepancy between LIA and DNS in the far field.

The budget data show that the modelling of the $\overline{u'e'}$ transport equation should focus on the dominant effects of the pressure–energy and pressure–dilatation terms, and can neglect the smaller effects of viscosity and nonlinear turbulence–turbulence interactions. The linear inviscid theory captures these inviscid phenomena and can be exploited for developing closure models for the source terms. A similar approach was employed for the study of the amplification of turbulence kinetic energy across a shock wave (Sinha *et al.* 2003). The linear inviscid mechanism of shock-unsteadiness damping was found to play a key role and was modelled based on LIA data. The shock-unsteadiness model was subsequently incorporated into one- and two-equation turbulence models, and successfully applied to shock/boundary-layer interactions; see, for example, Pasha & Sinha (2012). Note that LIA is able to match the pressure–dilatation effect in the budget of $\overline{u'e'}$ transport equation. The pressure–energy term is systematically overpredicted, the discrepancy increasing with Mach number, and a suitable correction to the LIA-based closure model may be required.

6. Summary

This paper presents a detailed study of the turbulent energy flux generated across a shock wave using linear interaction analysis and direct simulation data. The canonical interaction of homogeneous isotropic turbulence with a nominally normal shock wave is considered, and a purely vortical disturbance field is assumed upstream of the shock. We focus on the streamwise component of the turbulent energy flux and investigate the physics governing its magnitude and direction relative to the shock wave. In the framework of the linear theory, the upstream disturbance field is Fourier-decomposed into two-dimensional planar vorticity waves, each of which interacts independently with the shock.

The elementary interaction of individual vorticity waves provide fundamental understanding about the turbulent energy flux generated at the shock wave. The energy

flux correlation is a strong function of the shock strength and the angle of incidence of the upstream disturbance wave. At low Mach numbers, the majority of the waves yield negative $\overline{u'e'}$ in the near field, which implies energy transfer back towards the shock wave. The trend is opposite at high Mach numbers, where the near-field turbulent energy transfer is mostly directed away from the shock. Vorticity waves incident at small angles relative to the shock wave lead to propagating disturbances, with slowly varying turbulent energy flux behind the shock. On the other hand, plane wave interactions at high angles of incidence result in rapid postshock variation of $\overline{u'e'}$. Starting from a low near-field level, the correlation increases to a positive peak value, because of the decay of the negatively correlated acoustic-mode contributions.

Three-dimensional statistics computed by superposition of the individual single-wave solutions also show a rapid variation of the turbulent energy flux. It occurs in the acoustic-adjustment region behind the shock, and is identical to the trends observed in DNS data for a range of shock strength, turbulent Mach number and Reynolds number based on Taylor microscale. The downstream turbulent energy flux in DNS attains a peak positive value followed by a decay to low levels far away from the shock. In the absence of viscous effects, the linear theory predicts high asymptotic values of the energy flux in the far field. The far-field correlation is primarily composed of the vortical and entropy components of the disturbance field, while the near field is dominated by the acoustic mode generated at the shock wave. A budget computed using DNS data shows that the peak value of the energy flux correlation is governed by the pressure–energy and pressure–dilatation source terms in the $\overline{u'e'}$ transport equation. These are dominated by the acoustic mode, which is linear and inviscid in nature, and are reproduced well by linear interaction analysis. There is negligible effect of viscous and nonlinear terms in the transport equation on the overall budget.

The effect of entropy and acoustic disturbances in the incoming turbulence on the postshock turbulent heat flux is estimated using LIA. The focus is on estimating the magnitudes of these effects rather than the exact values, since different realistic flows have varying levels and correlations among the different disturbances. Despite clearly overestimating the amount of acoustic waves present in the DNS, LIA still suggests that the influence of these acoustic waves on the postshock turbulent heat flux is minimal. The entropy disturbances, on the other hand, are shown to potentially affect the postshock heat flux by about 10 % for the specific DNS case assessed here; this case had almost isentropic incoming turbulence, and thus the effect should be larger in flows with significant entropy disturbances, such as boundary-layer flows.

Overall, the linear theory is able to predict the peak turbulent heat flux in the DNS for weak shocks, and the Mach number scaling of $\overline{u'e'}$ in the hypersonic limit. There is also a qualitative match between LIA and DNS data for the entire range of shock strengths. In addition, LIA is able to capture the dominant acoustic mechanism in the budget that is responsible for the rapid postshock variation of the turbulent energy flux. Advanced physics-based turbulence models can thus be developed based on the linear inviscid theory to predict the peak positive turbulent energy flux behind a shock wave. When applied to shock/boundary-layer interaction, the positive values of the energy flux correlation would imply turbulent transfer of internal energy away from the shock. For cases where an oblique shock is inclined towards the wall, this can add significantly to the wall heat transfer rate. Examples include the reattachment shock in a compression corner interaction. Furthermore, the peak energy flux correlation occurs within one integral length scale of the downstream flow. This corresponds to about one boundary-layer thickness past the reattachment point, which is often the region with highest heat transfer to the wall.

Acknowledgements

Appendix A. Interaction of a vortical wave with normal shock

We present the details of linear interaction analysis applied to a vortical disturbance interacting with a normal shock. The development closely follows the work of Mahesh *et al.* (1996) and is reproduced here for completeness. In the linear inviscid framework, the shock-downstream variables are related to the shock-upstream values via the linearized Rankine–Hugoniot equations given in (2.3), and the expressions for the coefficients are

$$\left.\begin{array}{ll} B = \dfrac{(\gamma - 1)M_1^2 - 2}{(\gamma + 1)M_1^2}, & C = \dfrac{4}{(\gamma - 1)M_1^2 + 2}, \\[3mm] D = \dfrac{4\gamma M_1^2}{2\gamma M_1^2 - (\gamma - 1)}, & E = \dfrac{2(M_1^2 - 1)}{(\gamma + 1)M_1^2}. \end{array}\right\} \tag{A 1}$$

The planar waveforms for the velocity fluctuations in the region upstream of the shock are given in (2.2) and the velocity and temperature fluctuations downstream of the shock are given in (2.4). In order to solve for the postshock fluctuations, the downstream planar waveforms are substituted in the linearized Rankine–Hugoniot and linearized Euler equations to yield the values of the associated complex amplitudes. The solution obtained for the complex amplitude $\widetilde{L}$ associated with the shock speed (2.5) is given by

$$\widetilde{L} = \frac{-\cos\psi - \beta D \sin\psi - r\alpha D \cos\psi + Br\cos\psi}{E\tan\psi - \beta D - r(1 - B + \alpha D)\cot\psi}, \tag{A 2}$$

where

$$\alpha = \frac{1}{\gamma M_2^2 r}\left[\frac{k_r}{r\cos\psi - k_r}\right], \quad \beta = \frac{1}{\gamma M_2^2 r}\left[\frac{\sin\psi}{r\cos\psi - k_r}\right]. \tag{A 3a,b}$$

Here, M_2 is the mean flow Mach number downstream of the shock, and $k_r = \widetilde{k}/k$ is the ratio of the streamwise wavenumber of the downstream acoustic wave to the wavenumber of the upstream vorticity wave. The nature of the acoustic wavenumber $\widetilde{k}$ varies based on the angle of incidence of the upstream vorticity wave relative to the critical angle ψ_c given by (2.6). For $0 < \psi < \psi_c$, $\widetilde{k}$ is real and is given by

$$\frac{\widetilde{k}}{k} = \frac{U_1}{U_2}\frac{M_2}{1 - M_2^2}\left[-M_2\cos\psi + \sin\psi\sqrt{\cot^2\psi - \frac{U_2^2}{U_1^2}\left(\frac{1}{M_2^2} - 1\right)}\right]. \tag{A 4}$$

For $\psi_c < \psi < \pi/2$, $\widetilde{k}$ is complex $(\widetilde{k} = \widetilde{k}_r + \mathrm{i}\widetilde{k}_i)$, and its real and imaginary parts are given by

$$\left.\begin{aligned}\frac{\widetilde{k}_r}{k} &= -\frac{U_1}{U_2}\frac{M_2^2}{1 - M_2^2}\cos\psi, \\[2mm] \frac{\widetilde{k}_i}{k} &= \frac{U_1}{U_2}\frac{M_2}{1 - M_2^2}\sin\psi\sqrt{\frac{U_2^2}{U_1^2}\left(\frac{1}{M_2^2} - 1\right) - \cot^2\psi}.\end{aligned}\right\} \tag{A 5}$$

The complex coefficients corresponding to the downstream velocity and temperature fluctuations (see (2.4)) can be expressed in terms of $\widetilde{L}$ as

$$\widetilde{F} = \alpha D(\sin\psi - \widetilde{L}), \tag{A 6a}$$

$$\widetilde{G} = B\sin\psi + \widetilde{L}(1 - B) - \widetilde{F}, \tag{A 6b}$$

$$\widetilde{K} = D(\sin\psi - \widetilde{L}), \tag{A 6c}$$

$$\widetilde{Q} = C(\sin\psi - \widetilde{L}) - \widetilde{K}/\gamma. \tag{A 6d}$$

Using the above complex amplitudes, the velocity and temperature fluctuations at any given point in the shock-downstream region can be defined, and the turbulent energy flux can thus be calculated using (3.1), which is written again as

$$\overline{u_2' e_2'} = \left(\frac{1}{\gamma - 1}\right)\frac{1}{U_1 \overline{T}_2}\frac{\left[\overline{u_2' T_2'^*} + \overline{T_2' u_2'^*}\right]}{2(\mathrm{TKE}_1/U_1^2)}. \tag{A 7}$$

This corresponds to a single planar wave upstream of the shock wave. The three-dimensional value of turbulent energy flux can be obtained by integrating the incoming fluctuation over all the wavenumbers and angles of incidence for a specified upstream energy spectrum as shown in (A 8), which is same as (4.1) and is reproduced here for quick reference:

$$(\overline{u_2' e_2'})_{3D} = 4\pi\int_0^{\pi/2}\int_0^\infty (\overline{u_2' e_2'})_{2D}\,k^2\sin\psi\,\mathrm{d}k\,\mathrm{d}\psi. \tag{A 8}$$

The turbulent energy flux is normalized by the upstream turbulence kinetic energy TKE_1 as shown in (A 7). In a two-dimensional wave problem,

$$\mathrm{TKE}_1 = \frac{1}{2}\left[\overline{u_1'^2} + \overline{v_1'^2}\right] = \frac{|A_v|^2}{2}U_1^2, \tag{A 9}$$

where $\overline{u_1'^2} = \overline{u_1' u_1'^*}$ and $\overline{v_1'^2} = \overline{v_1' v_1'^*}$; subscript 1 corresponds to shock-upstream and $*$ indicates complex conjugate, with the expressions for u_1' and v_1' given in (2.2). In the case of three-dimensional interaction, the expression for shock-upstream turbulence kinetic energy is given by (Mahesh *et al.* 1996)

$$\mathrm{TKE}_1 = 4\pi U_1^2\int_0^{\pi/2}\int_0^\infty E(k)\sin\psi\,\mathrm{d}k\,\mathrm{d}\psi, \tag{A 10}$$

where $E(k)$ is the three-dimensional energy spectrum tensor given by (4.8).

Appendix B. Interaction of a vorticity–entropy wave with a normal shock

For a vorticity–entropy wave interacting with a normal shock, the upstream velocity fluctuations have the planar waveforms as given in (2.2). The upstream pressure fluctuations are identically zero and the upstream temperature and density fluctuations have the planar waveform as

$$
\frac{T_1'}{\overline{T}_1} = -\frac{\rho_1'}{\overline{\rho}_1} = -A_e \exp[\mathrm{i}k(x\cos\psi + y\sin\psi - U_1 t\cos\psi)],
\tag{B 1}
$$

where A_e represents the complex amplitude for the upstream entropy wave. The formulation is identical to that presented in Mahesh *et al.* (1996) and is reproduced here for completeness. The linearized Rankine–Hugoniot equations relating the fluctuations upstream and downstream of the shock can be expressed as

$$
\left.
\begin{aligned}
\frac{u_2' - \xi_t}{U_1} &= B\frac{u_1' - \xi_t}{U_1} + \check{B}\frac{T_1'}{\overline{T}_1}, \\
\frac{v_2'}{U_1} &= \frac{v_1'}{U_1} + E\xi_y, \\
\frac{\rho_2'}{\overline{\rho}_2} &= C\frac{u_1' - \xi_t}{U_1} + \check{C}\frac{T_1'}{\overline{T}_1}, \\
\frac{p_2'}{\overline{p}_2} &= D\frac{u_1' - \xi_t}{U_1} + \check{D}\frac{T_1'}{\overline{T}_1},
\end{aligned}
\right\}
\tag{B 2}
$$

where B, C, D and E are given by (A 1), and $\check{B}$, $\check{C}$ and $\check{D}$ are given as

$$
\check{B} = \frac{2}{(\gamma+1)M_1^2}, \quad \check{C} = -\frac{(\gamma-1)M_1^2 + 4}{(\gamma-1)M_1^2 + 2}, \quad \check{D} = -\frac{2\gamma M_1^2}{2\gamma M_1^2 - (\gamma-1)}.
\tag{B 3a–c}
$$

The expression for the complex amplitude $\widetilde{L}$ taking into account the upstream entropy fluctuations can be written as

$$
\widetilde{L} = \frac{-\cos\psi - \beta\left(D\sin\psi - \check{D}\dfrac{A_e}{A_v}\right) + r\cot\psi\left[-\alpha\left(D\sin\psi - \check{D}\dfrac{A_e}{A_v}\right) + B\sin\psi - \check{B}\dfrac{A_e}{A_v}\right]}{E\tan\psi - \beta D - r\cot\psi(1 - B + \alpha D)},
\tag{B 4}
$$

where α and β are given by (A 3). The ratio A_e/A_v can be expressed as $A_r\exp(\mathrm{i}\phi_r)$, where A_r and ϕ_r represent the amplitude ratio and the phase difference, respectively, between the upstream entropy and vorticity waves:

$$
A_r = \frac{\sqrt{\overline{\rho_1'^2}/\overline{\rho}_1}}{\sqrt{\mathrm{TKE}_1}/U_1}, \quad \phi_r = \cos^{-1}\left[\frac{\overline{u_1'\rho_1'}}{\sqrt{\overline{u_1'^2}}\sqrt{\overline{\rho_1'^2}}}\right].
\tag{B 5a,b}
$$

The values of A_r obtained for each of the DNS cases are shown in table 1. The complex amplitudes that govern the velocity and temperature fluctuations are given by $\widetilde{F}$, $\widetilde{G}$, $\widetilde{K}$ and $\widetilde{Q}$ as given by (2.4), and these can be expressed in terms of $\widetilde{L}$ as

$$
\widetilde{F} = \alpha D(\sin\psi - \widetilde{L}) - \alpha\check{D}\frac{A_e}{A_v},
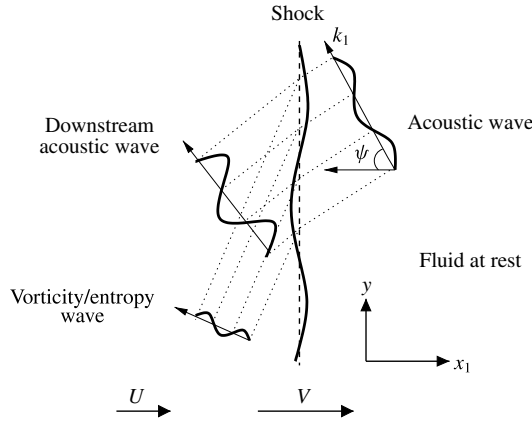\tag{B 6a}
$$

FIGURE 23. A single acoustic wave in a stationary gas interacts with a shock wave moving with a velocity V to generate all three waves (acoustic, entropy and vorticity).

$$\widetilde{G} = B \sin \psi + \widetilde{L}(1 - B) - \widetilde{F} - \check{B}\frac{A_e}{A_v}, \qquad (B\,6b)$$

$$\widetilde{K} = D(\sin \psi - \widetilde{L}) - \check{D}\frac{A_e}{A_v}, \qquad (B\,6c)$$

$$\widetilde{Q} = C(\sin \psi - \widetilde{L}) - \frac{\widetilde{K}}{\gamma} - \check{C}\frac{A_e}{A_v}. \qquad (B\,6d)$$

The energy flux correlation can then be obtained using (A 7) and (A 8).

Appendix C. Interaction of an acoustic wave with normal shock

Moore (1954) considered a shock moving with a velocity V into a stationary gas having an acoustic wave; a schematic is shown in figure 23. All three modes (acoustic, entropy and vorticity) are generated downstream of the shock, and the amplitude and phase of the downstream waves are functions of the angle of incidence and shock strength. In an alternative frame of reference, this configuration is similar to the one considered in the current study, where a mean flow convecting the disturbance interacts with a stationary shock wave. The development follows the work of Moore (1954) and all the essential steps required to obtain the results in §5.1 are given below.

In the frame of reference x_1–y (figure 23) attached to the fluid at rest, the upstream acoustic waveforms can be represented as

$$\frac{u_1'}{V} = -\frac{\cos \psi}{\gamma M_1} A_p \exp[ik_1(x_1 \cos \psi - y \sin \psi + a_1 t)], \qquad (C\,1a)$$

$$\frac{T_1'}{\overline{T}_1} = \frac{\gamma - 1}{\gamma} A_p \exp[ik_1(x_1 \cos \psi - y \sin \psi + a_1 t)], \qquad (C\,1b)$$

where u_1' is the streamwise velocity fluctuation in the stationary gas, V represents the mean shock velocity and T_1' is the temperature fluctuation; a_1 and $\overline{T}_1$ represent the mean speed of sound and temperature, respectively, in the gas which is stationary in

the mean; ψ represents the angle of incidence of the upstream acoustic wave with respect to the shock-normal direction, and k_1 is the corresponding wavenumber; A_p is the amplitude of the acoustic wave and $M_1 = V/a_1$ is the Mach number of the shock wave.

The downstream acoustic field could be either decaying or propagating in nature depending on the angle of the incident acoustic wave. The critical angles ψ_{cl} and ψ_{cu} are obtained as the roots of the following equation (Moore 1954):

$$\left(\frac{a_2}{V}\right)^2 - \left(1 - \frac{U}{V}\right)^2 = \left(\cot \psi + \frac{a_1}{V} \csc \psi\right)^2, \tag{C 2}$$

where a_2 and U are the postshock mean speed of sound and mean velocity, respectively. For upstream angles of incidence in the range $0 \leqslant \psi < \psi_{cl}$ or $\psi_{cu} < \psi \leqslant \pi$, the downstream acoustic wave has a propagating nature, and for $\psi_{cl} < \psi < \psi_{cu}$, the acoustic wave decays exponentially.

The linearized Rankine–Hugoniot conditions are now given as

$$\left. \begin{aligned} \frac{\xi_t - u'_2}{V} &= B\frac{\xi_t - u'_1}{V} + \hat{B}\frac{p'_1}{P_1}, \quad \frac{v'_2}{V} = \frac{v'_1}{V} - \frac{U}{V}\xi_y, \\ \frac{T'_2}{\overline{T}_2} &= (D - C)\frac{\xi_t - u'_1}{V} + (\hat{D} - \hat{C})\frac{p'_1}{\overline{p}_1}, \end{aligned} \right\} \tag{C 3}$$

where the terms B, C and D are as defined in (A 1). The coefficients due to the acoustic fluctuations are given as follows:

$$\hat{B} = \left(\frac{\gamma - 1}{\gamma + 1}\right)\frac{2}{\gamma M_1^2}, \quad \hat{C} = \frac{1}{\gamma}\left(1 - \frac{2(\gamma - 1)}{2 + (\gamma - 1)M_1^2}\right), \quad \hat{D} = \frac{2M_1^2 - (\gamma - 1)}{2\gamma M_1^2 - (\gamma - 1)}. \tag{C 4a–c}$$

The solutions for the downstream waveforms in the propagating regime ($0 \leqslant \psi_1 < \psi_{cl}$ or $\psi_{cu} < \psi_1 \leqslant \pi$) are given by

$$\frac{1}{A_p}\frac{u'_2}{V} = \widetilde{F}\exp(\mathrm{i}k_2\eta_a) + \widetilde{G}\exp(\mathrm{i}k_1\eta_v), \tag{C 5a}$$

$$\frac{1}{A_p}\frac{T'_2}{\overline{T}_2} = \frac{\gamma - 1}{\gamma}\widetilde{K}\exp(\mathrm{i}k_2\eta_a) - \widetilde{Q}\exp(\mathrm{i}k_1\eta_v), \tag{C 5b}$$

where the arguments of the vorticity/entropy waveform (η_v) and the acoustic waveform (η_a) are defined as

$$\left. \begin{aligned} \eta_a &= \alpha x_2 + \beta y + a_2 t, \\ \eta_v &= \frac{\cos\psi + 1/M_1}{1 - r}x_2 - y\sin\psi. \end{aligned} \right\} \tag{C 6}$$

The above downstream expressions are written in a frame of reference that moves with a mean velocity U such that the x_2 axis is stationary with respect to the mean flow downstream of the shock; k_2 is the corresponding downstream wavenumber.

The complex coefficients $\widetilde{K}$ and $\widetilde{F}$ correspond to the acoustic mode, $\widetilde{G}$ corresponds to the vortical mode and $\widetilde{Q}$ represents the contribution from the entropy mode.

The expressions for α, β, $\widetilde{K}$, $\widetilde{F}$, $\widetilde{G}$ and $\widetilde{Q}$ are provided below; they are functions of the upstream Mach number and the angle of incidence.

$$
\widetilde{L} = -\frac{m}{\gamma M_1}
$$

$$
\times \frac{\left[1 + \frac{\gamma+1}{4}\frac{M_1}{m}\left(\frac{3-\gamma}{\gamma+1} + \frac{\gamma-1}{2}r\right)\right]\chi + \frac{\gamma+1}{4}\left[1 - 2\frac{\gamma-1}{\gamma+1}\frac{n}{\sigma} - \frac{n\sigma}{1-r}\right](1-r)}{1 + \chi - \frac{\gamma+1}{4}r\left(1 + \frac{\sigma^2}{1-r}\right)},
$$

$$(C\,7)$$

$$
\widetilde{K} = D\left(\widetilde{L} + \frac{m}{\gamma M_1}\right) + \hat{D}, \quad \widetilde{Q} = C\left(\widetilde{L} + \frac{m}{\gamma M_1}\right) + \hat{C} - \frac{\widetilde{K}}{\gamma}, \tag{C\,8a,b}
$$

$$
\widetilde{F} = -\frac{a_2}{\gamma V}\widetilde{K}\alpha, \quad \widetilde{G} = \widetilde{L} - \widetilde{F} - B\left(\widetilde{L} + \frac{m}{\gamma M_1}\right) - \hat{B}, \tag{C\,9a,b}
$$

where

$$
l = \sin\psi, \quad m = \cos\psi, \quad n = \tan\psi, \tag{C\,10a-c}
$$

$$
r = \frac{2}{\gamma+1}\left(1 - \frac{1}{M_1^2}\right), \quad \left(\frac{a_2}{V}\right)^2 = (1-r)\left(1 + \frac{\gamma-1}{2}r\right), \quad \sigma = \frac{n(1-r)}{1 + \frac{1}{M_1 m}},
$$

$$(C\,11a-c)$$

$$
\chi = \left[1 - \frac{r(\gamma+1)(1+\sigma^2)}{2 + (\gamma-1)r}\right]^{1/2}, \quad \alpha = \frac{1}{1-r}\left[\frac{\lambda_2}{\lambda_1}\left(m + \frac{1}{M_1}\right) - \frac{a_2}{V}\right], \quad \beta = -l\frac{\lambda_2}{\lambda_1},
$$

$$(C\,12a-c)$$

$$
m\frac{\lambda_2}{\lambda_1} = m\frac{k_1}{k_2} = \frac{\frac{a_2}{V}\left(1 + \frac{1}{M_1 m}\right)}{\left(1 + \frac{1}{M_1 m}\right)^2 + n^2(1-r)^2}\left[1 + \sqrt{1 - r\frac{1 + n^2(1-r)^2\Big/\left(1 + \frac{1}{M_1 m}\right)^2}{1 - \frac{\gamma-1}{\gamma+1}(1-r)}}\right].
$$

$$(C\,13)$$

The solutions for the fluctuations in the decaying regime, i.e. $\psi_{cl} < \psi < \psi_{cu}$, are given as

$$
\frac{1}{A_p}\frac{u_2'}{V} = \widetilde{F}_{(1)}\Phi_{(1)} + \widetilde{F}_{(2)}\Phi_{(2)} + \left(\widetilde{G}_{(1)} + i\widetilde{G}_{(2)}\right)\exp(ik_1\eta_v), \tag{C\,14a}
$$

$$
\frac{1}{A_p}\frac{T_2'}{\overline{T}_2} = \frac{\gamma-1}{\gamma}\left(\widetilde{K}_{(1)}\Phi_{(1)} + \widetilde{K}_{(2)}\Phi_{(2)}\right) + \left(\widetilde{Q}_{(1)} + i\widetilde{Q}_{(2)}\right)\exp(ik_1\eta_v), \tag{C\,14b}
$$

where η_v is as defined before and the expressions for $\Phi_{(1)}$ and $\Phi_{(2)}$ are

$$\left.\begin{array}{l} \Phi_{(1)} = \exp(k_1\zeta)\,\exp(\mathrm{i}k_1\eta_d), \\ \Phi_{(2)} = \mathrm{i}\exp(k_1\zeta)\,\exp(\mathrm{i}k_1\eta_d), \end{array}\right\} \tag{C 15}$$

where the arguments ζ and η_d are given by

$$\zeta = d(x_2 - (V-U)t), \quad \eta_d = (\alpha x_2 + \beta y + cVt). \tag{C 16a,b}$$

The coefficients $\widetilde{K}_{(\alpha)}$ and $\widetilde{F}_{(\alpha)}$ correspond to the acoustic mode, $\widetilde{G}_{(\alpha)}$ to the vorticity mode, and $\widetilde{Q}_{(\alpha)}$ represents the entropy mode. The expressions for these amplitudes along with those for c, d, α and β are provided below.

$$\left.\begin{array}{l} \widetilde{L}_{(1)} = \dfrac{h_1 h_2 - \left(\dfrac{m}{\gamma M_1} + \dfrac{\hat{D}}{D}\right)h_3^2}{h_2^2 + h_3^2}, \quad \widetilde{L}_{(2)} = h_3\,\dfrac{h_1 + \left(\dfrac{m}{\gamma M_1} + \dfrac{\hat{D}}{D}\right)h_2}{h_2^2 + h_3^2}, \\[3mm] \widetilde{F}_{(1)} = h_4\left(\widetilde{L}_{(1)} + \dfrac{m}{\gamma M_1} + \dfrac{\hat{D}}{D}\right) - h_5\widetilde{L}_{(2)}, \\[3mm] \widetilde{F}_{(2)} = h_5\left(\widetilde{L}_{(1)} + \dfrac{m}{\gamma M_1} + \dfrac{\hat{D}}{D}\right) + h_4\widetilde{L}_{(2)}, \\[3mm] \widetilde{K}_{(1)} = D\left(\widetilde{L}_{(1)} + \dfrac{m}{\gamma M_1}\right) + \hat{D}, \quad \widetilde{K}_{(2)} = D\widetilde{L}_{(2)}, \\[3mm] \widetilde{Q}_{(1)} = C\left(\widetilde{L}_{(1)} + \dfrac{m}{\gamma M_1}\right) + \hat{C} - \dfrac{\widetilde{K}_{(1)}}{\gamma}, \quad \widetilde{Q}_{(2)} = C\widetilde{L}_{(2)} - \dfrac{\widetilde{K}_{(2)}}{\gamma}, \\[3mm] \widetilde{G}_{(1)} = \widetilde{L}_{(1)} - \widetilde{F}_{(1)} - B\left(\widetilde{L}_{(1)} + \dfrac{m}{\gamma M_1}\right) - \hat{B}, \quad \widetilde{G}_{(2)} = \widetilde{L}_{(2)}\,(1-B) - \widetilde{F}_{(2)}, \end{array}\right\} \tag{C 17}$$

where

$$\left.\begin{array}{l} h_1 = -\dfrac{1-r}{r}\dfrac{1}{\sigma}\left[\dfrac{l}{\gamma M_1} + \left(\dfrac{m}{\gamma M_1}B + \hat{B}\right)\dfrac{1}{\sigma}\right], \quad h_2 = 1 - \dfrac{1-r}{r}\dfrac{1-B}{\sigma^2}, \\[3mm] h_3 = -\dfrac{4d\,(1-r)\,/l\sigma}{2+(\gamma-1)\,r}, \quad h_4 = \dfrac{4}{\gamma+1}\dfrac{\sigma^2}{1+\sigma^2}, \quad h_5 = \dfrac{2rd\sigma\,(1-r)}{l\,(1+\sigma^2)}\dfrac{V^2}{a_2^2}, \\[3mm] c = \dfrac{m+1/M_1}{1 - V^2\,(1-r)^2\,/a_2^2}, \quad \alpha = -\dfrac{V^2}{a_2^2}\,(1-r)\,c, \quad \beta = -l, \\[3mm] d = \sqrt{\dfrac{\alpha^2 + l^2 - V^2c^2/a_2^2}{1 - V^2(1-r)^2/a_2^2}}, \end{array}\right\} \tag{C 18}$$

with l, m, n and σ being the same as in the propagating regime.

The normalized turbulent energy flux generated downstream of the shock can be written as

$$\overline{u_2' e_2'} = \left(\dfrac{1}{\gamma-1}\right)\dfrac{1}{V\overline{T}_2}\dfrac{\left[\overline{u_2' T_2'^*} + \overline{T_2' u_2'^*}\right]}{2(\mathrm{TKE}_1/V^2)}, \tag{C 19}$$

where the velocity fluctuation is normalized by the mean shock speed V, which is identical to the upstream mean flow velocity relative to the shock. The temperature fluctuation is normalized by the downstream mean temperature $\overline{T}_2$, and c_v is normalized by R. Here, * indicates complex conjugate.

Mahesh *et al.* (1995) extend the two-dimensional analysis by Moore (1954) to study a field of acoustic waves interacting with a shock. In the linear inviscid framework, the postshock statistics are computed by superimposing single-wave results for a specified isotropic energy spectrum upstream of the shock wave. The value of downstream $\overline{u'_2 e'_2}$ for a three-dimensional isotropic spectrum of planar waves can be written as

$$(\overline{u'_2 e'_2})_{3D} = 2\pi \int_0^\pi \int_0^\infty (\overline{u'_2 e'_2})_{2D}\, k^2 \sin\psi\, \mathrm{d}k\, \mathrm{d}\psi, \qquad (C\,20)$$

where $(\overline{u'_2 e'_2})_{2D}$ is the correlation obtained for a two-dimensional planar wave. Computations of the three-dimensional statistics require the spectrum of pressure fluctuations ahead of the shock, which is related to the three-dimensional energy spectrum $E(k)$ as

$$\frac{|\hat{p}_1|^2(\boldsymbol{k})}{\overline{p}_1^2} = \left(\frac{\gamma M_1}{V}\right)^2 \frac{E(k)}{4\pi k^2}, \qquad (C\,21)$$

with the expression for $E(k)$ taken as per the von Karman spectrum given in (4.8). Further details are provided in Mahesh *et al.* (1995).

REFERENCES

BOWERSOX, R. D. W. 2009 Extension of equilibrium turbulent heat flux models to high-speed shear flows. *J. Fluid Mech.* **633**, 61–70.

BRINCKMAN, K. W., CALHOON, W. H. JR & DASH, S. M. 2007 Scalar fluctuation modeling for high-speed aeropropulsive flows. *AIAA J.* **45** (5), 1036–1046.

CAMBON, C., COLEMAN, G. N. & MANSOUR, N. N. 1993 Rapid distortion analysis and direct simulation of compressible homogeneous turbulence at finite Mach number. *J. Fluid Mech.* **257**, 641–665.

DURBIN, P. A. & ZEMAN, O. 1992 Rapid distortion theory for homogeneous compressed turbulence with application to modeling. *J. Fluid Mech.* **242**, 349–370.

FABRE, D., JACQUIN, L. & SESTERHENN, J. 2001 Linear interaction of a cylindrical entropy spot with a shock. *Phys. Fluids* **13** (8), 2403–2422.

GOLDBERG, U. C., PALANISWAMY, S., BATTEN, P. & GUPTA, V. 2010 Variable turbulent Schmidt and Prandtl number modeling. *Engng Appl. Comput. Fluid Mech.* **4**, 511–520.

GRIFFOND, J. 2005 Linear interaction analysis applied to a mixture of two perfect gases. *Phys. Fluids* **17**, 086101.

GRIFFOND, J., SOULARD, O. & SOUFFLAND, D. 1993 Reynolds stress model fitted to match linear interaction analysis predictions. *Phys. Scr.* **T142**, 014059.

HANIFI, A. E., ALFREDSSON, P. H., JOHANSSON, A. V. & HENNINGSON, D. S. 1999 *Transition, Turbulence and Combustion Modelling*, ERCOFTAC Series.

JACQUIN, L., CAMBON, C. & BLIN, E. 1993 Turbulence amplification by a shock wave and rapid distortion theory. *Phys. Fluids.* A **5**, 2539–2550.

KOVASZNAY, L. S. G. 1953 Turbulence in supersonic flow. *J. Aeronaut. Sci.* **20** (10), 657–674.

LARSSON, J., BERMEJO-MORENO, I. & LELE, S. K. 2013 Reynolds- and Mach number effects in canonical shock-turbulence interaction. *J. Fluid Mech.* **717**, 293–321.

LARSSON, J. & LELE, S. K. 2009 Direct numerical simulation of canonical shock-turbulence interaction. *Phys. Fluids* **21**, 126101.

LEE, S., LELE, S. K. & MOIN, P. 1993 Direct numerical simulation of isotropic turbulence interacting with a weak shock wave. *J. Fluid Mech.* **251**, 533–562.

LEE, S., LELE, S. K. & MOIN, P. 1997 Interaction of isotropic turbulence with shock waves: effect of shock strength. *J. Fluid Mech.* **340**, 225–247.

MAHESH, K., LEE, S., LELE, S. K. & MOIN, P. 1995 The interaction of an isotropic field of acoustic waves with a shock wave. *J. Fluid Mech.* **300**, 383–407.

MAHESH, K., LELE, S. K. & MOIN, P. 1996 The interaction of a shock wave with a turbulent shear flow, *Tech. Rep.* 69. Thermosciences Division, Department of Mechanical Engineering, Stanford University, Stanford, CA.

MAHESH, K., LELE, S. K. & MOIN, P. 1997 The influence of entropy fluctuations on the interaction of turbulence with a shock wave. *J. Fluid Mech.* **334**, 353–379.

MENTER, F. R. 1994 Two-equation eddy-viscosity turbulence models for engineering applications. *AIAA J.* **32** (8), 1598–1605.

MOORE, F. K. 1954 Unsteady oblique interaction of a shock wave with a plane disturbances, *NACA Tech. Rep. 1165*.

MORKOVIN, M. V. 1962 Effects of compressibility on turbulent flows. In *Mécanique de la Turbulence* (ed. A. Favre), pp. 367–380. CNRS.

PASHA, A. A. & SINHA, K. 2008 Shock-unsteadiness model applied to oblique shock-wave/turbulent boundary-layer interaction. *Intl J. Comput. Fluid Dyn.* **22** (8), 569–582.

PASHA, A. A. & SINHA, K. 2012 Shock-unsteadiness model applied to hypersonic shock-wave/turbulent boundary-layer interactions. *J. Propul. Power* **28** (1), 46–60.

POPE, S. B. 2000 *Turbulent Flows*. Cambridge University Press.

RIBNER, H. S. 1953 Convection of a pattern of vorticity through a shock wave, *NACA Tech. Rep.* TN-2864.

RIBNER, H. S. 1954 Shock-turbulence interaction and the generation of noise, *NACA Tech. Rep.* 1233.

RISTORCELLI, J. R. & BLAISDELL, G. A. 1997 Consistent initial conditions for the DNS of compressible turbulence. *Phys. Fluids* **9** (1), 4–6.

ROY, C. J. & BLOTTNER, F. G. 2001 Review and assessment of turbulence models for hypersonic flows. *Prog. Aerosp. Sci.* **42** (7), 469–530.

RYU, J. & LIVESCU, D. 2014 Turbulence structure behind the shock in canonical shock-vortical turbulence interaction. *J. Fluid Mech.* **756**, R1.

SCHULEIN, E. 2006 Optical skin friction measurements in short-duration facilities. *AIAA J.* **44**, 1732–1741.

SINHA, K. 2012 Evolution of enstrophy in shock/homogeneous turbulence interaction. *J. Fluid Mech.* **707**, 74–110.

SINHA, K., MAHESH, K. & CANDLER, G. V. 2003 Modeling shock-unsteadiness in shock-turbulence interaction. *Phys. Fluids* **15**, 2290–2297.

SINHA, K., MAHESH, K. & CANDLER, G. V. 2005 Modeling the effect of shock unsteadiness in shock-wave/turbulent boundary-layer interactions. *AIAA J.* **43** (3), 586–594.

SOMMER, T. P., SO, R. M. C. & ZHANG, H. S. 1993 Near-wall variable-Prandtl-number turbulence model for compressible flows. *AIAA J.* **31** (1), 27–35.

THIVET, F., KNIGHT, D. D., ZHELTOVODOV, A. A. & MAKSIMOV, A. I. 2001 Importance of limiting the turbulent stresses to predict 3D shock-wave/boundary-layer interactions. In *23rd International Symposium on Shock Waves, Ft. Worth, TX, Paper No.* 2761, p. 7.

VEERA, V. K. & SINHA, K. 2009 Modelling the effect of upstream temperature fluctuations on shock/homogeneous turbulence interaction. *Phys. Fluids* **21**, 025101.

WILCOX, D. C. 2008 Formulation of the k–ω turbulence model revisited. *AIAA J.* **46** (11), 2823–2838.

WOUCHUK, J. G., DE LIRA, C. HUETE RUIZ & VELIKOVICH, A. L. 2009 Analytical linear theory for the interaction of a planar shock wave with an isotropic turbulent vorticity field. *Phys. Rev. E* **79**, 066315.

XIAO, X., HASSAN, H. A., EDWARDS, J. R. & GAFFNEY, R. L. JR. 2007 Role of turbulent Prandtl numbers on heat flux at hypersonic Mach numbers. *AIAA J.* **45** (4), 806–813.